Dynamics of settling-driven convection beneath a sediment-laden buoyant overflow: implications for the length-scale of deposition in lakes and the coastal ocean

Journal:	*Sedimentology*
Manuscript ID	SED-2018-OM-085.R1
Manuscript Type:	Original Manuscript
Date Submitted by the Author:	n/a
Complete List of Authors:	Davarpanah Jazi, Shahrzad; University of Toronto, Physical and Environmental Sciences Wells, Mathew; University of Toronto, Physical and Environmental Sciences
Keywords:	Sediment-laden gravity current, Settling-driven convection, Turbidity currents, Density ratio, Stokes settling velocity, Overflow

Note: The following files were submitted by the author for peer review, but cannot be converted to PDF. You must view these files (e.g. movies) online.

MovieS1.wmv
MovieS2.wmv
MovieS3.wmv
MovieS4.wmv
MovieS5.wmv
MovieS6.wmv

SCHOLARONE™
Manuscripts

1   **Dynamics of settling-driven convection beneath a sediment-laden buoyant overflow:**
2   **implications for the length-scale of deposition in lakes and the coastal ocean**
3
4
5
6
7   Shahrzad Davarpanah Jazi and Mathew G. Wells
8   Department of Physical & Environmental Sciences, University of Toronto
9   1065 Military Trail, M1C 1A4, Toronto, ON, Canada
10   Email: sh.davarpanahjazi@mail.utoronto.ca, Email: wells@utsc.utoronto.ca
11
12
13
14
15

16   **ABSTRACT**
17   A series of laboratory experiments were conducted in order to determine how settling-driven
18   convection influences the length-scale over which the majority of particles settle beneath a
19   buoyant sediment-laden plume spreading over a denser saline layer. This system is analogous to
20   sediment-laden river water spreading into a lake or the coastal ocean. The key dimensionless
21   parameter that controls the settling dynamics of such flows is the density ratio, defined as the
22   ratio of density differences due to the added salt and sediment. For a buoyant plume, this ratio
23   has to be greater than unity, so that the experiments in the current study were performed for
24   density ratios between one and five. When density ratio was close to one, settling-driven
25   convection was vigorous and the length-scale over which sedimentation occurred was very
26   small. A strong secondary turbidity current was generated in this case. On the other hand, for
27   larger values of density ratio, the predicted length-scale over which a secondary plume was
28   generated increased proportional with the density ratio. A complete mathematical expression for
29   this length-scale was developed using recent theory that described the time-scale over which
30   settling-driven convection evolved. The theoretically predicted propagation length-scale showed
31   very good quantitative agreement with laboratory experiments. The use of the dimensionless
32   density ratio allows the expression to predict which sediment-laden river plumes in lakes and the
33   coastal ocean could quickly form secondary turbidity currents.
34
35
36
37

38   **Keywords:** Sediment-laden gravity current, settling-driven convection, turbidity currents,
39   density ratio, Stokes settling velocity, overflow.

1   **INTRODUCTION**

2

3   Rivers are the main pathways by which sediment is transported to the coastal regions of lakes

4   and the ocean (Mulder & Syvitski, 1995). In a lake, a sediment-laden river is often denser than

5   the receiving waters and so can readily plunge and form a turbidity current, as originally

6   observed in pioneering work by Forel (1885) in Lake Geneva. In contrast, when a river flows

7   into the coastal ocean, the buoyant density difference between the fresh and saline water is

8   usually far greater than the unstable density difference due to the suspended sediment load.

9   Hence, almost all sediment-laden rivers will form surface plumes in the coastal ocean (Mulder &

10   Syvitski, 1995). The processes that control the length-scale over which sediment deposits

11   beneath these buoyant sediment-laden plumes is thus a key geological question. This length-

12   scale of deposition is directly related to the length-scale that the buoyant plume propagates

13   before losing all its sediment from beneath. Such length-scale has been described as the product

14   of the horizontal velocity of the buoyant plume and a time-scale over which sediment is lost

15   (Geyer *et al.*, 2004; Hill *et al.*, 2000). The horizontal velocity of a surface plume is well

16   understood (Yuan & Horner-Devine, 2017), and in the absence of strong winds or tides, it is

17   largely determined by buoyancy forces (Horner-Devine *et al.*, 2015). The time-scale over which

18   sedimentation occurs has been the focus of recent work by Hoyal *et al.* (1999b), Burns &

19   Meiburg (2012, 2015) and Davarpanah Jazi & Wells (2016), who identified settling-driven

20   convection as the potentially dominant fluid dynamical process that can rapidly transport

21   sediment from beneath sediment-laden buoyant plumes. Previous experiments (Maxworthy,

22   1999; Parsons *et al.*, 2001; Snow & Sutherland, 2014; Sutherland *et al.,* 2018) and direct

23   observations of buoyant surface sediment-laden plumes (Hughes Clarke *et al.*, 2014; Hizzett *et*

24   *al.*, 2017) showed that under certain conditions, the rapid sediment loss beneath such plumes can

25   generate a secondary turbidity current, which could provide an important mechanism to transport

26   sediment to the depths of the ocean from the continental margin. For instance, direct field

27   monitoring by Clare *et al.* (2016) has revealed that 70% of observations of the triggering of

28   secondary turbidity currents were linked to the sediment-laden plume in Howe Sound near the

29   Squamish River in BC, Canada. Since sediment-laden gravity currents are one of the main

30   mechanisms for transporting sediments into the deep ocean, where deep sand layers can form

31   (Meiburg & Kneller, 2010), this study aims to use laboratory experiments to quantify the

1　　conditions that can enhance sedimentation beneath such buoyant river plumes. Particularly, this

2　　study identifies the specific conditions that could potentially result in the formation of secondary

3　　turbidity currents from the many rivers in the coastal ocean that usually have low sediment loads

4　　and would almost always form surface plumes rather than plunging underflows (Mulder &

5　　Syvitski, 1995).

6

7　　　　The length-scale over which a surface plume propagates and loses sediment will give a first-

8　　order estimate of the distribution of sediment deposition from a river mouth, as illustrated

9　　schematically in Figure 1. If there are no currents beneath the surface plume, then the distance at

10　　which all of the sediment has fallen out of the plume determines the zone of deposition. If the

11　　concentrations are high enough, this depositing sediment could also potentially form a secondary

12　　turbidity current. Intuitively, the extent of propagation over which sediment is lost (L_{prop}) can be

13　　approximated as follows:

14

15　　$$L_{prop} = U T_S = U(\overline{H}/w_S) \tag{1}$$

16

17　　where U is the horizontal velocity of the buoyant plume and T_S is the time-scale over which

18　　particles settle through the moving surface plume. If particles are only being lost by a slow

19　　settling rate over the mean thickness of the plume $(\overline{H})$, then the settling time-scale is simply

20　　determined as $T_S = \overline{H} / w_S$, where w_S is the Stokes settling velocity of the sediment particles

21　　(Geyer $et\ al.$, 2004; Hill $et\ al.$, 2000). The horizontal velocity of a buoyant plume (U) is a

22　　function of the reduced gravity (g') between the plume and ambient and the thickness at the

23　　plume head (H). Thus, this velocity is given by $U = \mathrm{Fr}\ (g'H)^{1/2}$, where the reduced gravity is

24　　defined as $g' = g\ \Delta\rho / \rho$, with g the gravitational acceleration (9.81 m s^{-2}) and $\Delta\rho$ and ρ are

25　　respectively the density difference and average density between the current and the saline

26　　ambient with units of kg m^{-3}. The Froude number is the key dimensionless parameter for

27　　describing gravity current dynamics and is defined as $\mathrm{Fr} = U / (g'H)^{1/2}$. Essentially the Froude

28　　number compares the observed speed to that of an internal wave speed. Numerous experimental

29　　studies have consistently found the Froude number to be order one (i.e. Turner, 1979; Simpson,

30　　1982; Gladstone & Pritchard, 2010; Snow & Sutherland, 2014), which is close to the value of 1 /

31　　$\sqrt{2}$ found in theoretical studies (Benjamin, 1968; Huppert, 2006; Meiburg & Kneller, 2010).

1   Recent direct numerical simulations of buoyant double-diffusive gravity currents by Penney &

2   Stastna (2016) have suggested that a no-slip condition (representing a solid lid) may increase

3   drag compared to a free-slip condition (representing an air-water interface), and hence they

4   would predict different Fr than for buoyant plumes compared to regular bottom gravity currents.

5

6   Using typical values for laboratory and field situations, Equation (1) predicts very large

7   propagation length-scales if the only settling process considered is Stokes settling velocity. For

8   instance a typical gravity current in a laboratory experiment with a strong buoyancy difference,

9   has a speed of order $U \sim 0.1$ m s^{-1}. The mean thickness of a typical laboratory gravity current is

10   of order $\overline{H} = 0.1$ m. Hence, using for example Silicon Carbide (SiC) sediment particles of size

11   7.8×10^{-6} m with Stokes settling velocity of $w_S = 7.7 \times 10^{-5}$ m s^{-1}, implies a settling time of $T_S =$

12   1300 s. Therefore, assuming that the current is moving at 0.1 m s^{-1}, it would need to propagate

13   the very large distance of 130 m for all the particles to settle out of the plume, and hence

14   laboratory plumes with fine sediment might be predicted to propagate to the end of any realistic

15   experimental tank before losing all of their sediment. In contrast, previous laboratory

16   experiments have found that settling-driven convection is much more important than just the

17   Stokes settling velocity, so that laboratory plumes with fine sediment particles can lose sediment

18   at much faster rates (Maxworthy, 1999; Parsons *et al.*, 2001; Snow & Sutherland, 2014,

19   Sutherland *et al.,* 2018). The scaling in Equation (1) assumes that particles are settling in a

20   laminar manner within the gravity current. If the flow is turbulent however, so that the

21   concentration is well mixed, then the average mass concentration (C with units of kg m^{-3}) in the

22   flow changes with time as $C(t) = C_o e^{(-t\,W_s/\overline{H})}$ (Martin & Nokes, 1988; Sparks *et al.*, 1991),

23   where C_0 is the initial mass concentration of the flow (kg m^{-3}). With such an exponential decay,

24   95% of particles settle out after three settling time-scales, i.e. an even greater distance is implied

25   by Equation (1).

26

27   There are a number of mechanisms by which the time-scale used in Equation (1) could be

28   much smaller than that predicted from the Stokes settling velocity of a single particle, including

29   flocculation (Rouhnia & Strom, 2015, 2017) and settling-driven convection (Burns & Meiburg,

30   2012, 2015). This study will focus on the potential role of settling-driven convection, as the

31   description of increased settling rates due to flocculation is now quite mature (Rouhnia & Strom,

1   2015, 2017). Several field observations have found that sediment is lost from a buoyant plume at

2   rates much faster than predicted by the Stokes settling velocity. For instance, Nowacki *et al.*

3   (2012) computed the sediment removal rate from the Colombia River, USA and determined that

4   the settling rate (10 mm s^{-1}) was substantially larger than the settling velocity of a single particle

5   (2 mm s^{-1}). Similarly, Scheu *et al.* (2015) used acoustic backscatter measurements beneath a

6   river plume in a thermally stratified lake, to infer increases of an order of magnitude over the

7   Stokes settling velocities of the suspended sediments settling from turbid river plumes. In the

8   absence of flocculation, the most likely potential mechanism for these increased sedimentation

9   rates is settling-driven convection, the vigour of which depends on the unstable sediment

10   contrast between the layers.

11

12   Settling-driven convection is an important instability that can occur when a layer of fresh

13   sediment-laden water lies above a layer of saline water (Fig. 2). Initially this configuration can

14   be stable if the mean density of the upper layer is less than that of the lower layer (as shown in

15   Figure 2A). However, as sediment settles through the saline interface, a layer of particle rich

16   fluid forms that contains both salt and sediment, and is now denser than the fluid below (the nose

17   region in Figure 2B). Since this layer is unstable, convection of sediment-laden plumes begins

18   (Fig. 2C). These dense sediment-laden finger-like plumes sink with vertical velocities that are 10

19   to 100 times larger than Stokes settling velocity (Hoyal *et al.*, 1999b; Burns & Meiburg, 2012,

20   2015; Davarpanah Jazi & Wells, 2016). This process is highly important to Equation (1), as it

21   suggests that a much shorter time-scale T_s is relevant for sediment-laden buoyant plumes, so that

22   the deposition length-scale will be far less than predicted by only assuming Stokes settling

23   velocity of a single particle. Such finger-like plumes have been seen in a number of studies

24   (Bradly, 1965; Hoyal *et al.*, 1999b) and this process is seen to greatly increase the particle

25   removal rate from an otherwise buoyant upper layer (Houk & Green, 1973; Green, 1987; Chen,

26   1997; Hoyal *et al.*, 1999a, b; Maxworthy, 1999; Parsons & Garcia, 2000; Parsons *et al.*, 2001;

27   Davarpanah Jazi & Wells, 2016). Recent work by Davarpanah Jazi & Wells (2016) showed that

28   in a salt/sediment configuration with no horizontal velocities, the vigour of convection was

29   dictated by density ratio defined as $R_\rho = \Delta\rho_S / \Delta\rho_C$, the ratio of density differences due to the

30   added salt ($\Delta\rho_S$) and sediment ($\Delta\rho_C$). For a sediment-laden layer of fresh water to float above a

31   saline layer, R_ρ must be greater than one. The most vigorous convection was found to occur for

1   marginal stability when R_ρ was very close to one. Theoretical and numerical studies of settling-

2   driven convection (Burns & Meiburg, 2012, 2015; Yu *et al.*, 2013, 2014; Shao *et al.*, 2017) have

3   quantified the time-scales for these processes, and revealed the internal dynamics of the velocity

4   fields that are difficult to see experimentally.

5

6   One of the key findings of the previous experiments and field observations on buoyant

7   sediment-laden plumes is that settling-driven convection is an important mechanism for moving

8   sediments rapidly from surface plumes to the lake or ocean bed, where dense secondary turbidity

9   currents can potentially form (Maxworthy, 1999; Parsons *et al.*, 2001; Snow & Sutherland, 2014;

10   Hughes Clarke *et al.,* 2014; Sutherland *et al.,* 2018). As almost all sediment-laden river plumes

11   are initially buoyant, many papers have cited Parsons *et al.* (2001) to suggest settling-driven

12   convection could be a key process by which turbidity currents can be formed in the coastal ocean

13   near river mouths, which ultimately transport sediment to deep regions of the ocean (Meiburg &

14   Kneller, 2010). It is very challenging in a field study to isolate the specific mechanism by which

15   secondary turbidity currents can be generated from a buoyant sediment-laden plume (Gales et al.,

16   2018), and only a limited number of field studies have attempted to investigate this process (see

17   for example optical backscatter measurements of Hughes Clarke *et al.* 2014, Kineke *et al.* 2000

18   and Hill *et al.* 2008). This has placed great importance to these earlier experiments, especially

19   Parsons *et al.* (2001). In the current study, the aim is to revisit these earlier experiments, and

20   improve the understanding on processes that set the length-scale in Equation (1) in light of the

21   recent improvements to the theoretical understanding of the time-scales of settling-driven

22   convection (Burns & Meiburg, 2012, 2015; Yu *et al.*, 2013, 2014; Shao *et al.*, 2017).

23   Specifically, this paper aims to extend the initial study of Maxworthy (1999) by applying the

24   time-scale used in Burns & Meiburg (2012, 2015) to determine how the length-scale in Equation

25   (1) varies as a function of density ratio (R_ρ).

26

27   The experiments in this paper aim to quantify how settling-driven convection could control

28   the length-scale of deposition beneath a buoyant plume, and isolate the specific conditions under

29   which secondary turbidity currents can form. As this process is challenging to study in the field,

30   the presented experimental visualizations of such processes will help geologists to better

31   conceptualize field observations. Using the most recent results from modelling of settling-driven

1   convection, a new equation is developed to describe the distance over which sediment is lost due

2   to settling-driven convection. There is excellent agreement between the quantitative theory and

3   the laboratory results. The paper ends with an extrapolation of the findings of this study to

4   predict the relevant length-scales for river plumes entering the coastal ocean.

5

6   **EXPERIMENTAL DESIGN**

7

8   In order to better understand how the process of settling-driven convection controls deposition

9   beneath buoyant plumes in lakes and the coastal ocean, a series of experiments were performed,

10   where a controlled volume of sediment-laden fluid was released into a large tank that contained a

11   well-mixed saline solution (Fig. 3). The large tank had dimensions of $1.83 \times 0.55 \times 0.305$ m, and

12   sediment-laden fluid was initially contained behind a removable metal barrier in a compartment

13   of dimensions $0.35 \times 0.115 \times 0.23$ m. The two compartments were the same temperature, as they

14   were both filled with tap water stored in large vessels that had equilibrated with room

15   temperature (18.5 ± 2.3 °C). Keeping the temperature constant throughout all experiments,

16   resulted in a two-component salt/sediment configuration similar to experiments of Maxworthy

17   (1999). The ambient saline solution was prepared from high purity food grade salt. The sediment

18   used in the experiments was Silicon Carbide (SiC) grinding powder with a density of $\rho_{SiC} = 3210$

19   kg m^{-3}. This material is monodispersed and non-cohesive and was previously used in the

20   experiments of Maxworthy (1999), Hoyal *et al.* (1999b), Davarpanah Jazi & Wells (2016) and

21   Sutherland *et al.* 2018. The median diameter of particles was 7.8×10^{-6} m, resulting in a

22   predicted Stokes settling velocity of 7.7×10^{-5} m s^{-1}.

23

24   In these experiments, the salinity contrast between the surface plume and the ambient fluid

25   was kept constant, and the sediment concentration was increased. Thus, the density ratios varied

26   from $R_\rho = \infty$ (no sediment) to $R_\rho = 1$ (neutral stability). The cases where $R_\rho < 1$ would have the

27   sediment being denser than the ambient fluid so would immediately form underflows. The

28   density of the saline ambient (ρ_S) was kept constant at 1002.5 ± 0.4 kg/m^3, while the amount of

29   sediment added to surface plume was varied. The different densities of sediment-laden water (ρ_C)

30   were obtained by adding various masses of sediment ($0 \leq m_C \leq 0.065$ kg) to the fixed volume of

31   fresh water within the small compartment. The mass of sediment was determined using an Ohaus

1   SPX222 balance (Ohaus Corporation, Parsippany, NJ, USA) with precision of 10^{-2} g. The

2   densities of saline water (ρ_S) and the water in the compartment, before adding sediment (ρ_{comp}),

3   were measured using an Anton Paar DMA 35 Ex portable densitometer (Anton Paar USA Inc.,

4   Ashland, VA, USA) with an accuracy of $\pm\ 10^{-3}$ g cm^{-3} and a resolution to 10^{-4} g cm^{-3}. The

5   temperatures (t_S and t_{comp}) were measured simultaneously with the same instrument to the

6   precision of 0.2 °C.

7

8   The density of a fluid can be determined as $\rho_f = \rho_0 + \Delta\rho_S + \Delta\rho_C$ and is linearly related to both

9   concentrations of salt and sediment. Here, ρ_0 is the density of clear fresh water at 20°C (998.2 kg

10   m^{-3}). The added density due to the added salt was calculated using $\Delta\rho_S = \rho_S - \rho_{comp}$, where the

11   density of fresh water in the compartment is $\rho_{comp} = 999.1 \pm 0.2$ kg m^{-3}. The density anomaly due

12   to the added sediment was calculated as $\Delta\rho_C = \gamma\ C\ \rho_{comp}$, in which γ is the density expansion

13   coefficient for SiC particles defined as ($\rho_{SiC} - \rho_{comp}$) / ρ_{SiC}. Furthermore, φ is the mass

14   concentration of sediment particles (kg kg^{-1}) denoted by $\varphi = m_C / (m_C + m_{comp})$, where the mass

15   of the water in the small compartment (m_{comp}) was determined as $m_{comp} = \rho_{comp}\ V_{comp}$, in which

16   V_{comp} was the volume of the compartment (m^3).

17

18   The entire tank was initially filled with saline water with density ρ_S, and then the barrier was

19   inserted to isolate the smaller compartment. With the use of two small pumps, the saline water in

20   this compartment was replaced with freshwater, by discharging salt water out and pumping fresh

21   water in simultaneously. An equivalent of four times the volume of the small compartment was

22   replaced in order to guarantee that 99% of the saline water was flushed out (Zhixin *et al.*, 2014).

23   An electrical mixer was used to keep the fluid well-mixed while being replaced.

24

25   The sediment particles were then added to the fresh water in the small compartment and a

26   well-mixed constant volume of sediment-laden water was prepared. The electrical mixer kept the

27   fluid stirred to inhibit the settling of particles and the total time between addition of sediment and

28   removal of barrier was kept to less than two minutes. Each experiment commenced with the

29   gentle removal of the metal barrier 10 s after the mixer was turned off to prevent turbulent

30   motion it produced within the fluid. In addition, food dye was added to the sediment water to

31   further improve flow detection. Digital cameras were used to capture the behaviour of the flow

1   from different angles through photos and movies. Two large LED light panels provided bright

2   and uniform lighting at the background in order to produce clear, sharp photos and movies from

3   the sediment-laden gravity current in motion.

4

5   A total of 19 experiments with density ratios in the range of $0.687 \leq R_\rho \leq \infty$ were performed.

6   Full details of all 19 experiments, including R_ρ, m_C, L_{prop} and the behaviour of sediment-laden

7   overflows, are summarized in Table 1. The six supplemental movies are available online and are

8   representative of the major trends in the behaviour of the current. In this table the experiments

9   are in an ascending order based on their density ratio. The experiment with $R_\rho = \infty$ (Movie S6 in

10   the Supplemental section) had no sediment, and the one experiment with $R_\rho = 0.687$ (Movie S1

11   in the Supplemental section) had sediment load such that it was initially denser than saline

12   ambient; all the other 17 experiments were initially positively buoyant and were in the range

13   $1.021 \leq R_\rho \leq 4.575$. The above two experiments ($R_\rho = \infty$ and 0.687) were performed only for

14   comparison purposes, as the main focus of this study was on sediment-laden overflows. The

15   propagation length-scale of the gravity current (L_{prop}) was measured by visually determining the

16   distance at which the thickness of the gravity current became less than 0.01 m and had

17   essentially stopped. The error bars in the determinations of L_{prop} represent an estimate of the

18   distance over which the gravity current changes from 0.02 m to 0 m thickness.

19

20   **THEORY**

21

22   Settling-driven convection can lead to far greater loss of sediments than Stokes settling, so

23   that use of Equation (1) would predict a much smaller and more realistic deposition length-scale.

24   In this section, the scaling of L_{prop} is now modified to take into account theoretical scaling of the

25   sedimentation time-scale, introduced by Burns & Meiburg (2012, 2015) to show how the density

26   ratio (R_ρ) and the stratification influence the propagation length-scale. In order to use Equation

27   (1) a horizontal velocity (U) and a sedimentation time-scale (T_S) are needed. For the former, the

28   horizontal velocity of the plume is a function of the reduced gravity, which can be expressed in

29   terms of the contribution of sediment and salt density anomalies as,

30

$$U = \mathrm{Fr}\left(\frac{g\,H}{\rho}\left(-\Delta\rho_C + \Delta\rho_S\right)\right)^{1/2} \tag{2}$$

1

where $\Delta\rho_S$ and $\Delta\rho_C$ are the added density due to the added salt and mass fraction of sediment respectively. By introducing the definition of density ratio ($R_\rho = \Delta\rho_S / \Delta\rho_C$) previously used by Davarpanah Jazi & Wells (2016), this velocity can be rewritten in terms of density ratio (R_ρ) and Froude number (Fr) as,

$$U = \mathrm{Fr}\left(\frac{g\,\Delta\rho_S}{\rho}H\left(1-\frac{1}{R_\rho}\right)\right)^{1/2} \tag{3}$$

The sedimentation time-scale (T_S) is determined by the dynamics of the instability at the interface between sediment-laden and saline fluid (Burns & Meiburg, 2015). The downward settling of sediment particles from the fresher layer into the denser saline layer (Fig. 2A) drives the settling-driven convection instability. A very thin layer of fluid, just below the interface containing both salt and sediment, forms a "nose" of unstable stratification with length-scale (L_C), as shown in Figure 2B. The convective instability at the base of the sediment-laden fluid is controlled by this thin "nose" region, as there is an unstable density inversion due to accumulation of settling sediment from above (Burns & Meiburg, 2012). When this layer grows sufficiently large, the dense material will sink as a convective plume (Fig. 2C). The numerical simulations of Burns & Meiburg (2012, 2015) and Shao *et al.* (2017) have shown that within the thin nose region of thickness L_C, the fluid dynamics are dominated by viscosity. This implies that both Grashof number and Reynolds number are equal to one at the point just before instability occurs.

The Grashof number is defined as,

$$\mathrm{Gr} = \frac{g'_C\, L_C^3}{v^2} \tag{4}$$

where $g'_C = g\,\Delta\rho_C / \rho_0$ is the reduced gravity defined in terms of the density difference due to the added sediment ($\Delta\rho_C$) and density of fresh water (ρ_0) (Burns & Meiburg, 2012, 2015) and $v = 10^{-6}$ m^2 s^{-1} is the coefficient of kinematic viscosity of fresh water at 20 $^\circ$C. In this region, a Reynolds number can also be defined as,

1

$$Re = \frac{w_S L_C}{v} \tag{5}$$

3

4 where the vertical velocity of fluid in this layer is assumed to be the same as the settling velocity

5 w_s (Shao *et al.,* 2017).

6

7 The important time-scale for convective instability can be derived through the following steps.

8 First, assuming Re = 1 implies that

9

$$L_C = \frac{v}{w_S} \tag{6}$$

11

12 Similarly assuming that in the viscosity dominated unstable nose region Gr = 1 results in a

13 scaling for the thickness of the nose region in terms of the viscosity and reduced gravity as,

14

$$L_C = \left(\frac{v^2}{g_C'}\right)^{1/3} \tag{7}$$

16

17 Note that g'_C is the reduced gravity defined in terms of the density difference due to the added

18 sediment ($\Delta\rho_C$) and density of fresh water (ρ_0). By equating Equations (6) and (7), the settling

19 velocity within the convectively unstable nose region is shown to be related to the reduced

20 gravity of the sediment layer and viscosity as,

21

$$w_S = (g_C' v)^{1/3} \tag{8}$$

23

24 Therefore using Equation (6), the time-scale ($T_C = L_C / w_s$) for a particle of velocity w_S to fall

25 into the unstable nose region of thickness L_C would be given by,

26

$$T_C = \left(\frac{v}{g'_C{}^2}\right)^{1/3} \tag{9}$$

28

1 Note that this expression does not contain the Stokes settling velocity (w_S). This resulting time-

2 scale (T_C), is the fundamental time-scale for the convective sedimentary instability, and has been

3 used in a number of important recent studies to non-dimensionalize the time-scales of various

4 numerical simulations (Burns & Meiburg 2012, 2015; Shao *et al.,* 2017).Their resulting 3D

5 simulations suggest that it takes of order 100 time-scales for fully developed settling-driven

6 convection to develop. This convective time-scale will subsequently be used in this paper to

7 determine the experimental length-scale over which sediment is lost from the bottom of a surface

8 plume. From this point onwards, c_t will be defined as the dimensionless multiple of the time in

9 Equation (9) that takes for settling-driven convection to develop, and the value of c_t will be

10 determined experimentally. It will be assumed that the sedimentary convective time-scale of

11 Burns & Meiburg (2012, 2015) is the relevant time-scale for sediment to be lost from the sharp

12 density interface beneath the overflow so that $T_S = T_C$. With this assumption, Equations (3) and

13 (9) can be combined to estimate a propagation length-scale (L_{prop}) for the gravity current as,

14

15
$$L_{prop} \sim \text{Fr} \left(g\frac{\Delta\rho_S}{\rho_0}H\left(1 - \frac{1}{R_\rho}\right) \right)^{1/2} v^{1/3} \left(g\frac{\Delta\rho_C}{\rho_0} \right)^{-2/3} \qquad (10)$$

16

17   To see the dependence on R_ρ even more clearly, by keeping the salinity anomaly $\Delta\rho_S$ constant

18 and assuming Fr ~ 1, then two dimensional constants are introduced, $c_1 = (g\,\Delta\rho_S\,H\,/\,\rho_0)^{1/2}$ and c_2

19 $= v^{1/3}\,(g\,\Delta\rho_S\,/\,\rho_0)^{-2/3}$, with units of m s^{-1} (speed) and s (time) respectively. This reduces the

20 propagation length-scale to a simple function of R_ρ as,

21

22
$$L_{prop} = c_1 c_2 c_t \left(1 - \frac{1}{R_\rho}\right)^{1/2} R_\rho^{2/3} \qquad (11)$$

23

24 where the combined coefficients $c_1 c_2$ (assuming $\rho \approx \rho_0$) can be furthermore simplified to provide

25 a scale constant (with units of m) as,

26

27
$$c_1 c_2 = H^{1/2}\, v^{1/3} \left(g\frac{\Delta\rho_S}{\rho}\right)^{-1/6} \qquad (12)$$

28

29 The propagation length-scale (L_{prop}) in Equation (11) goes to zero as R_ρ approaches unity (when

30 there is no density difference between the two layers) and it increases as $R_\rho^{2/3}$ for large R_ρ. For

1　the case of $R_\rho < 1$ an underflow would occur as the plume would be initially denser than the

2　receiving environment.

3

4　**RESULTS**

5

6　**Evolution of the current is related to density ratio**

7　　The striking differences in the behaviour of the sediment-laden current can be seen in the

8　photograph time series from experiments (Figs. 4, 5 and 6). In particular, the propagation length-

9　scale of the plume is a strong function of the density ratio and decreases as R_ρ gets close to one.

10　Secondary turbidity currents are also seen to form most strongly as R_ρ gets close to unity. In all

11　cases, the changes in behaviour are tied to the vigour of settling-driven convection that strongly

12　increases as R_ρ decreases towards unity.

13

14　　The speed at which sediment-laden plumes sink beneath the surface plume increases

15　dramatically with decreasing R_ρ (Fig. 4). The series of photographs in Figure 4 depicts the

16　behaviour of the overflow every 30 s for $R_\rho = 3.051$ and 1.48 (left and right panels respectively).

17　The higher value $R_\rho = 3.051$ in Figures 4A to 4J means there is less sediment, and results in weak

18　settling-driven convection. On the other hand for a smaller density ratio of $R_\rho = 1.48$, Figures 4K

19　to 4T depicts a very vigorous mode of settling-driven convection, which resulted in the rapid

20　sinking of distinct finger-like structures. Figures 4J and 4Q display evidence of settling to the

21　bottom after 270 s and 180 s respectively. These corresponds to vertical velocities of

22　approximately $w = 0.14 \times 10^{-3}$ m s^{-1} for $R_\rho = 3.051$, whereas for $R_\rho = 1.48$ the vertical velocity is

23　faster with $w = 2.2 \times 10^{-3}$ m s^{-1}. For comparison, the Stokes settling velocity of an individual

24　particle is 7.7×10^{-5} m s^{-1}, and hence the estimated time from the Stoke settling velocity for a

25　single SiC particle to go from the top to the bottom of the experimental tank is 2 hr. Thus, Figure

26　4 shows that settling-driven convection at low density ratios has a substantial effect on

27　increasing the downward velocity of collections of SiC particles.

28

29　　The shapes of the sinking sediment-laden fingers also change with increasing density ratio as

30　displayed in Figure 5. These close-up images illustrate the reduction in width and velocity of the

31　convective sediment fingers as density ratio increases. Figure 5 displays zoomed in photos, taken

14

1   every 30 s, and shows weaker settling-driven convection for R_ρ = 4.575 and a much more

2   vigorous settling-driven convection for R_ρ = 1.229. The vertical distance moved by fingers

3   between images indicate faster velocities for R_ρ = 1.229, where the fingers of sediment were

4   wider and formed earlier (compared to R_ρ = 4.575). The vertical velocity of the small plumes (for

5   R_ρ = 4.575) and the large fingers (for R_ρ = 1.229) can be estimated as $w = 6 \times 10^{-4}$ m s^{-1} and $w =$

6   3×10^{-3} m s^{-1} respectively (similar to Figure 4). A general trend in both Figures 4 and 5 is that as

7   density ratio decreases towards unity, the surface current moved slower horizontally and the

8   formation of finger-like structures occurred earlier. With the increase in the mass of particles for

9   lower R_ρ, the sediment settled faster as well as entraining water out of the current (as described

10   before by Maxworthy (1999) and Sutherland et $al.$ (2018)). Therefore, the head of the current

11   decreased in size and could eventually stop before the end of the tank if settling-driven

12   convection was vigorous enough.

13

14   In many experiments, the intense settling-driven convection could form a turbid interflow or

15   an intense turbidity current beneath the buoyant plume (Fig. 6). The series of photos in Figure 6,

16   taken every 60 s, displays these two distinct behaviours of flow for R_ρ = 1.172 and R_ρ = 1.054. In

17   both cases the current moved visibly slower (in the horizontal direction) than those discussed

18   earlier in Figure 5. As can be seen in Figure 6, both currents never reached the end of the tank

19   and stopped before passing 1.5 m, as the sediments settled rapidly due to the very vigorous

20   settling-driven convection of SiC particles. In Figures 6E to 6J, corresponding to R_ρ = 1.172,

21   after the overflow stopped at L_{prop} = 1.3 m, it was interesting to observe the emergence of an

22   interflow below the initial overflow, which lasted for a long time. In this case not only the

23   sediment particles were falling down but they were also dragging water down with them.

24   However, these plumes were not heavy enough to plunge down to the very bottom of the tank.

25   Therefore, the amount of water that the plume carried with itself became significant (similar

26   observations are reported in Sutherland et $al.$ 2018). On the other hand, for R_ρ = 1.054 the

27   overflow stopped at a shorter distance of L_{prop} = 0.75 m and an underflow occurred shortly after.

28   This formation of a secondary underflow is consistent with observations first made by

29   Maxworthy (1999).

30

31   **Horizontal propagation of the current is related to density ratio**

1   The difference between the horizontal velocities of the buoyant plumes with various density

2   ratios can be determined from a series of horizontal photos of the top 0.127 m of the overflow

3   (Fig.7). The standard equation for the velocity in a buoyant plume (Eq. 3) predicted that the

4   horizontal velocity would scale with density ratio as $U \sim (1 - 1 / R_\rho)^{1/2}$, i.e. the velocity decreases

5   as R_ρ approaches one, where there is no density difference. Equation (3) is governed by the

6   dimensionless Froude number, which has usually been found to be between 0.5 to 1 in many

7   previous experiments (i.e. Turner, 1979; Simpson, 1982; Gladstone & Pritchard, 2010; Snow &

8   Sutherland, 2014). As an illustration of this, three cases of $R_\rho = \infty$, 2.492 and 1.172 are

9   considered here. The speed of the overflow was determined by fitting the best line to the front of

10   the current in each stack of images. The speeds corresponding to the density ratios under

11   consideration were $U_{(R\rho = \infty)} = 0.0279$ m s^{-1}, $U_{(R\rho = 2.492)} = 0.0246$ m s^{-1} and $U_{(R\rho = 1.172)} = 0.0068$ m

12   s^{-1}. Note that for $R_\rho = 1.172$ the gravity current stopped at $L_{prop} = 1.3$ m, as was also displayed in

13   Figure 6. The comparison of the initial speed of the propagating overflow in the three figures

14   shows a faster speed for the larger density ratios, consistent with the scaling of Equation (3).

15   Using the observed experimental speeds, Equation (3) then determines the Froude number for R_ρ

16   $= \infty$ to be Fr$_{(R\rho = \infty)} = 0.820$. Furthermore, estimations of the Froude number based on Equation (3)

17   for $R_\rho = 2.492$ and 1.172 are Fr$_{(R\rho=2.492)} = 0.880$ and Fr$_{(R\rho=1.172)} = 0.506$ respectively. These

18   estimates of the dimensionless Froude numbers are all within the expected range of 0.5 to 1 from

19   previous experiments (i.e. Turner, 1979; Simpson, 1982; Gladstone & Pritchard, 2010). It is also

20   noteworthy in Figure 7 that in all three cases there appears to be no influence from the end wall

21   on these estimates of propagation speed, as the horizontal velocity is constant with time up to the

22   point where plumes hit the wall.

23

24   There is very good quantitative agreement between the theoretical prediction of Equation (11)

25   and experimental results of the propagation length-scale of the sediment-laden gravity current as

26   a function of density ratio (Fig. 8). This is the most important result in this paper, and Figure 8

27   shows that the propagation length-scale decreases to zero as density ratio decreases to one. For

28   R_ρ less than one a plunging flow would occur. The data points are surrounded by two curves in

29   blue, which provides upper and lower bounds on the constants c_1 and c_2 in Equation (12). For

30   experimental conditions in the current study, where 2.9 kg m^{-3} $\leq \Delta\rho_S \leq$ 3.7 kg m^{-3}, the two

31   constants are in the range of $0.0380 \leq c_1 \leq 0.0619$ m s^{-1} and $0.0967 \leq c_2 \leq 0.1848$ s, so that the

1   product of $c_{1avg}\,c_{2avg} = 0.0069$ m. As outlined earlier, previous numerical simulations of Burns &

2   Meiburg (2012, 2015) suggest that it will take several hundred time-scales for large "finger"

3   instabilities to develop, and so in Figure 8 the blue theoretical curves are plotted to have values

4   of $c_t = 440$ and 500. These two values bracket the observations well and are consistent with the

5   expectation that c_t is of order 100. For typical values of c_1 and c_2 in laboratory conditions, with 1

6    $< R_\rho < 2$, the propagation length-scale is predicted to be $0 < L_{prop} \leq 1.83$ m. Furthermore, for any

7    $R_\rho > 1.3$ in the conducted experiments the observed propagation length-scale (L_{prop}) was limited

8   to the tank length of 1.83 m. It is important to note that all these observations have length-scales

9   dramatically smaller than the prediction of L_{prop} based on the Stokes particle settling rate in

10   Equation (1). The much smaller length-scale is a direct result of the increase rate of particle loss

11   under the influence of settling-driven convection process.

12

13   **DISCUSSION**

14

15   **Density ratio predicts the sedimentation pattern**

16   The fluid dynamics of the convective sedimentation beneath a buoyant river plume are

17   strongly influenced by the density ratio, as summarized in Figure 9. In the experiments with

18   lower sediment concentrations ($R_\rho > 2$), weak settling-driven convection and slow sinking of

19   particles (e.g. $w = 6 \times 10^{-4}$ m s^{-1}) were observed, in experiments that lasted for a long duration of

20   time (e.g. t = 45 min). On the other hand, when $1.3 < R_\rho < 2$ fingers of sediment were rapidly

21   sinking with much greater vertical velocities of $w = 0.3 \times 10^{-3}$ m s^{-1} under the direct effect of

22   strong and vigorous settling-driven convection. In both of the above-mentioned cases the current

23   reached the end wall, so that $L_{prop} = 1.83$ m for these experiments in Figure 8. For higher

24   sediment concentrations with $1.17 < R_\rho < 1.23$, the surface plume stopped well before reaching

25   the end wall. In these cases, a slow moving sediment-laden interflow occurred beneath the

26   surface plume. Finally, for cases where R_ρ was very close to unity not only the surface flow

27   stopped, but also an intense underflow was observed. In a much longer tank, it is likely that all

28   the flows would have stopped, and hence formed some sort of subsurface gravity current.

29   However, it is noteworthy that the only intense secondary underflow occurred when $R_\rho \sim 1$. It is

30   very challenging to interpret isolated field observations beneath a river plume. Hence, the images

31   and animations of these various experiments (Supplementary material) when combined with

1   field estimates of R_ρ could provide a useful guidance for interpretation of data and the possible

2   design of future field observation campaigns.

3

4   The most important results of the current set of experiments is that Equation (11) quantifies

5   the length-scale over which it is likely that a surface sediment-laden plume can transform into a

6   subsurface turbidity current (Fig. 10). In lakes with smaller lengths than L_{prop} the sediment is

7   expected to rain down uniformly over the lake bed, possibly with some size fractionation with

8   larger particles closer to river mouth. However, if L_{prop} is sufficiently small compared to the size

9   of the lake, then a secondary turbidity current could form and deposit sediments far from the

10   river mouth, which are often ponded in the deepest regions of the basin. These two forms of

11   sedimentation will result in quite different stratigraphy in lake beds, which can then be used to

12   infer paleoclimate records of inflow events (Gilbert & Butler, 2004; Cossu *et al*., 2015).

13

14   The mechanism of transforming a buoyant sediment-laden plume into a secondary turbidity

15   current was first expressed by Maxworthy (1999) and greatly popularized in the sedimentology

16   literature by Parsons *et al*. (2001). This process is often invoked as a potential mechanism by

17   which turbidity currents can form, given that typically sediment loads in rivers are not high

18   enough to directly form underflows (Mulder & Syvitski, 1995; Mulder & Chapron, 2011).

19   Equation (11) can now be used to rigorously quantify when secondary turbidity currents are

20   likely to form. The experimental observations and theoretical predictions in this study confirm

21   that the propagation length-scale of such a flow can dramatically change once density ratio gets

22   very close to unity and it scales as $L_{prop} \sim (1 - 1 / R_\rho)^{1/2} \, R_\rho^{2/3}$. When R_ρ is less than one, an

23   underflow would form. It is expected that sediment-laden river inflows into lakes will typically

24   have much lower density ratios than in the coastal ocean, so that the behaviour of sedimentation

25   and deposition scales will be very different for the same sediment load in a river (Fig. 9). When a

26   river flows into a lake, the density difference arises due to the temperature anomaly (rather than

27   the salinity difference). The largest density anomaly expected in most lakes might be a 20 °C

28   river flowing into a 10 °C lake, so that $g \, \Delta\rho_S / \rho = 0.0146$ m s^{-2}. In contrast, for a fresh river

29   entering the ocean saline water the reduced gravity would be of order $g \, \Delta\rho_S / \rho = 0.294$ m s^{-2}, i.e.

30   at least 20 times greater. Thus, for the same sediment load, R_ρ is always much larger than one in

31   the ocean and much closer to one in a lake. Underflows are frequently observed in rivers entering

1   lakes (see for example Fig.19D-2 in Talling *et al.* 2013, and Cossu *et al.* 2015), whereas only

2   very rarely do rivers have enough sediment load in the ocean to form underflows (Mulder &

3   Syvitski, 1995; Mulder & Chapron, 2011). As an example, Hughes Clarke *et al.* (2014) describe

4   typical sediment concentrations as usually being less than 0.07 kg m^{-3} in the Squamish River. In

5   the coastal ocean this is clearly insufficient to form an underflow directly, and the estimated

6   density ratio would be $R_\rho \sim 25$ kg m^{-3} / 0.07 kg m^{-3} ~ 350. In contrast, if this same river flowed

7   into a thermally stratified lake with a large 10 °C difference across the thermocline, it would

8   have $R_\rho \sim 1.5$ kg m^{-3} / 0.07 kg m^{-3} ~ 20, and could potentially even have $R_\rho \sim 1$, if the

9   temperature difference between river and lake was less than 1 °C. For $R_\rho \gg 1$ then $L_{prop} \sim R_\rho^{2/3}$,

10   so the difference in propagation length between $R_\rho = 20$ and 350 is a factor of 100, indicating a

11   substantial difference in the likely deposition behaviour between a lake and the ocean.

12

13   **From laboratory experiments to the field**

14   The idea from Parsons *et al.* (2001) that settling-driven convection can lead to formation of

15   turbidity currents has been often invoked to explain field observations of turbidity currents, but

16   only a few field studies detail some of the causal links. For instance, Hizzett *et al.* (2017) noted

17   that the occurrence of turbidity current below the delta of the Squamish River correlated best

18   with the presence of sediment-laden river plumes, rather than slope failures on the delta. In

19   addition, Schue *et al.* (2015) studied a sediment-laden river plume flowing into a thermally

20   stratified Alpine lake, and observed (using acoustic backscatter) that the vertical velocity of a

21   descending sediment layer below a river plume was an order of magnitude greater than Stokes

22   settling velocities, consistent with the experimental plumes in Figure 4. Furthermore, Giovanoli

23   (1990) studied the transport of sediments from Rhône River flowing into Lake Geneva as an

24   interflow. As mentioned in this study, the sediment concentration in the Rhône River is in the

25   range of 10 – 5000 mg l^{-1}. With the assumption that there is a 10 °C temperature difference

26   between the two layers, it would result in a density ratio within the range of $0.3 < R_\rho < 150$ ($R_\rho \sim$

27   1.5 kg m^{-3} / 5 kg m^{-3} ~ 0.3 and $R_\rho \sim 1.5$ kg m^{-3} / 0.01 kg m^{-3} ~ 150). When $R_\rho < 1$ in Rhône River

28   underflows would form, while for $1 < R_\rho < 150$ there is the potential that settling-driven

29   convection could be important underneath the Rhône River.

30

31   **Application of experimental results to river flows into the coastal ocean**

1   Rivers only occasionally have sufficient suspended sediment to have a density that exceeds

2   that of sea water, when they would immediately form plunging flows (Mulder & Syvitski, 1995).

3   Faster flowing rivers are able to erode and carry more sediment, so it is expected that if

4   underflows could form, it is during flooding events. Empirical data has often be used to find a

5   relationship between the suspended sediment concentration (C_s with units of kg m^{-3}) and the flow

6   rate of the river (Q with units of m^3 s^{-1}) of the form

7

8    $$C_S = a\, Q^b \qquad (13)$$

9

10   where a and b are empirical rating coefficients. Furthermore, Mulder & Syvitski (1995) show

11   that the increased concentration of sediment during a flood ($C_{s\ Flood}$) is related to the average

12   concentration $C_{s\ Average}$ as

13

14   $$C_{S\ Flood} = C_{S\ Average} \left(\frac{Q_{Flood}}{Q_{Average}} \right)^b \qquad (14)$$

15

16   where Q_{Flood} and $Q_{Average}$ are the flow rates during a flood and average conditions. An underflow

17   would occur if $C_s > \Delta\rho_{SeaWater}$. For typical 15 ºC and 35 ppt salinity seawater the density

18   difference with fresh water is $\Delta\rho_{SeaWater} = 25.9$ kg m^{-3} and hence, an underflow happens when C_s

19   > 25.9 kg m^{-3}. Mulder & Syvitski (1995) show that a large number of "moderately dirty" rivers

20   could produce underflows (i.e. $R_\rho < 1$) with $b < 1$ (Table 3 in Mulder & Syvitski 1995). For

21   "moderately clean" rivers on the other hand, many would need to have $1 < b \leq 1.5$ (Table 4 in

22   Mulder & Syvitski 1995) to occasionally produce underflows, whereas "relatively clean" rivers

23   would need $1.5 < b \leq 2$ (Table 5 in Mulder & Syvitski 1995) to ever be able to form underflows.

24

25   One of the key results of this experiment was to identify that there is a distance over which a

26   surface buoyant plume would lose most of its sediment. Hence, rather than an underflow

27   requiring that a river be denser than seawater, previous papers have suggested that settling-

28   driven convection should allow the sediment in many rivers to be able to convert to a turbid

29   underflow (i.e. Parsons *et al.,* 2001). In order to use the scaling of Equation (14) to estimate the

30   length-scale of propagation of a buoyant plume, the density ratio can be re-written as

31

$$R_\rho = \frac{\Delta\rho_S}{\Delta\rho_C} = \frac{\Delta\rho_{SeaWater}}{C_{S\,Flood}} \times \left(\frac{Q_{Average}}{Q_{Flood}}\right)^b \qquad (15)$$

Therefore, while the condition of Mulder & Syvitski (1995) requires $R_\rho \leq 1$ for underflow formation, the experiments conducted in this study show that in many cases a secondary turbidity current can form in a distance that increases with R_ρ.

It is helpful to consider when there might be sufficient sediment load in the Squamish River in BC, Canada to form underflows (Fig. 11). This particular river is a good example of a sediment-laden river that is known to form periodic underflows (Hizzett *et al.* 2017). Data from Table 3 in Mulder & Syvitski (1995) suggests that $C_{s\,Average}$ = 1 kg m^{-3}, $Q_{Average}$ = 58 m^3 s^{-1} and $b \leq 1$ for this river. In this case, assuming $b = 1$, then when Q_{Flood} = 1502 m^3 s^{-1}, the ratio Q_{Flood} / $Q_{Average}$ = 25.9 would predict R_ρ = 1. Any higher flow rate would have $R_\rho < 1$ and so for all higher values of Q a plunging flow would form. For normal flow conditions however, the density of suspended sediment is $C_{s\,Average}$ = 1 kg m^{-3}, which would predict R_ρ = 25.9. Hence, it is instructive to plot the predicted length-scale (L_{prop}) as a function of flow rate values (Q) in Figure 11. In this figure, depth of the river is assumed to be H = 10 m (note that the constant in Equation (11) depends on $H^{1/2}$ and hence the result is not very sensitive to exact choice of this values, which would also fluctuate with tides). In Using Equation (11), the predicted length-scale of deposition for the Squamish River is 136 m for the average flow rate value of $Q_{Average}$ = 58 m^3 s^{-1}, and up to 1 - 2 km for lower flow rate values (Fig. 11). While there are no direct observations of settling-driven convection below the Squamish River, the predicted length-scales of 100s to 1000s of meters are broadly consistent with the distributions of sediment from the Squamish River within Howe Sound (i.e. Figure 2 in Gales *et al.* 2018). The exact relationship between R_ρ and Q for a specific river would require more research – for instance the average value of observed suspended sediment concentrations made by Hughes Clarke *et al.* (2014) was 0.07 kg m^{-3} in the Squamish River, notably less than the value of $C_{s\,Average}$ = 1 kg m^{-3} described by Mulder & Syvitski (1995).

Important differences between laboratory experiments and the field

The real world is much more complicated than the idealized experiments performed in this paper. The major benefit of laboratory experiments is that they can be used to study one specific process in isolation so that the controlling parameters can be quantified. On the other hand, the

1   disadvantage is that when applying such scaling of the length-scale to a field setting, there may

2   be many other processes that could also be important. Hence, it is critical to discuss the

3   significant differences that might influence the interpretation of results in this paper. One

4   important difference is that the current set of experiments had a finite volume of sediment-laden

5   fluid that entered the ambient - these are the so-called "dam break" experiments and are widely

6   used in fluid dynamics laboratory experiments (i.e. Turner, 1979; Simpson, 1982; Gladstone &

7   Pritchard, 2010). A real river however has a constant inflow, with new material continuously

8   being pushed out from the river mouth. Therefore, even if most of the sediment is settling out

9   from the river plume in a distance L_{prop}, the surface layer would still be pushed out by the

10   continuous supply of water. Hence, the surface plume could continue to move out into the water

11   body many kilometers, even after settling has occurred. Thus, the length-scales shown in Figure

12   11B are probably lower bounds on what the length-scale of the surface plume would look like in

13   the field. In addition, Equation (11) implicitly assumes that the plume only spreads in one

14   dimension, as in the laboratory. This is probably a reasonable assumption for the Squamish River

15   spreading in the long fjord of Howe Sound, but in many coastal settings, river plumes are

16   unconstrained and will spread in two-dimensions (Horner-Devine *et al.*, 2015). Secondary

17   turbidity currents are also more likely to occur when there is a sloping bottom, as opposed to the

18   uniform depth in these experiments. For instance the experimental setup in the studies made by

19   Parsons *et al.* (2001), Snow & Sutherland (2014) and Sutherland *et al.* (2018) all included a

20   sloping ramp, which would probably increase the tendency to form turbidity currents beneath an

21   overflow.

22

23   Another critical process that occurs when fine river sediments meet the ocean is flocculation,

24   which can also dramatically increase settling rates as flocs of particles sink faster than an

25   individual particle. Flocculation is typically promoted at the pycnocline due to ionic exchange

26   and other processes, so where fresh water enters a saline body, flocculation may be more likely.

27   The increases in settling of sediment particles by flocculation could be occurring at the same

28   time as settling-driven convection, so future work would need to determine the relative

29   importance of such processes in estuaries. In real rivers there will also be a distribution of

30   sediment particle size, rather than the uniform particles used in this study. Larger particles can

31   sink into the "nose region" of Figure 2B faster than small particles, so there is weak dependence

on the instability time-scale of Equation (9), as observed in the 3D simulations of Burns & Meiburg (2015) and experimental observations of Sutherland *et al.* (2018). While some numerical work (i.e., Burns & Meiburg, 2012, 2015; Yu *et al.*, 2014, 2015) and experimental studies (Sutherland *et al.*, 2018) have suggested a weak dependence of the vigour of settling-driven convection on particle size, this remains an important area of future work. The main effect of a particle distribution will be some degree of fractionation of particles, with the larger particles being deposited closer to river mouth, and smaller particles settling at great differences from river mouth.

Tidal currents have also been shown to be somewhat important in triggering of turbidity currents in locations in British Columbia such as the Squamish River (Clare *et al.,* 2016) and the Fraser delta (Ayranci *et al.,* 2012; Lintern *et al.,* 2016). While Clare *et al.* (2016) found that surface sediment-laden plumes at Squamish were linked to ~70% of all turbidity currents; the precise timing was also strongly affected by tidal elevation. At low tides at Squamish, more (and coarser) sediment was flushed off the delta top, which increased the sediment flux and had higher settling rate due to coarser grains being transported. This tidal influence overprints the original signature of river discharge (Clare *et al.,* 2016). At low tides, it is also possible that the shallow water depth may also promote formation of turbidity currents as there would be less dilution of the sediment-laden convective fingers, similar to how the sloping ramp promoted the formation of turbidity currents in experiments of Parsons *et al.* (2001), Snow & Sutherland (2014) and Sutherland *et al.* (2018).

Possible applications of experiments to other systems

A recent paper by Stack *et al.* (2018) has tried to extrapolate some of the dynamics of sediment-laden rivers on Earth to understand ancient geological formations on Mars that possibly formed underwater. Specifically when trying to explain the geology of the Murray formation they speculate about the conditions under which an ancient Martian river could form an underflow in the Gale crater. A starting point for their discussion is that the evidence for geological deposits associated with a plunging river plume implies that the density of the river water be greater than that of the receiving waters (i.e. that $R_\rho \leq 1$). From various estimates of the possible sediment load in river they draw inferences as to how salty the water body could

1   have been. The analysis in this paper hopefully shows that in many situations plunging

2   underflows can also form for $R_\rho > 1$ due to the active settling-driven convection at the base of the

3   overflow. Hence, the estimates by Stack *et al.* (2018) of the salinity of ancient water bodies in

4   the Gale crater are possibly lower bounds, which have important implications for life on Mars.

5

6   A final area where the dynamics of settling-driven convection is relevant is in the dynamics of

7   pyroclastic flows, especially in how a hot volcanic ash cloud might intrude into the thermally

8   stratified atmosphere. Indeed the current work is related to previous experiments of Carazzo &

9   Jellinek (2012, 2013), Manzella *et al.* (2015) and Scollo *et al.* (2017), who studied the dynamics

10   of settling-driven convection in order to interpret field observations of ash-laden volcanic clouds.

11   In particular, geologists often wish to know the radius over which ash will deposit, as this has

12   important hazard prediction implications. Equation (11) could be used to help estimate this

13   radius – the major difference being that the air has a much lower viscosity than water, which will

14   tend to enhance the rate at which the instability forms. The video imagery provided in the

15   Supplementary material might further help interpret the finger like sediment plumes often seen in

16   field observations of volcanic ash clouds (Scollo *et al.,* 2017).

17

18   **CONCLUSION**

19

20   The main finding of this paper is that settling-driven convection can result in the rapid loss of

21   sediment below a buoyant plume. The length-scale of sediment deposition is determined by the

22   length-scale over which the plume propagates, and the faster sediment loss due to settling-driven

23   convection results in a far smaller propagation length-scale compared to a simple estimate made

24   by the Stokes settling velocity. The vertical settling of dense sediment-laden plumes was

25   measured to be as much as 100 times that of the Stokes settling velocity of an individual particle.

26   For density ratios close to unity, the propagation length-scale was small and an intense

27   underflow or interflow emerged, which propagated longer distance than the surface plume.

28   However, when density ratio was larger than one this length-scale increased as $R_\rho^{2/3}$. For a given

29   salt stratification in an estuary, or thermal stratification in a lake, the sediment difference

30   between the surface and deep layers will determine the strength of settling-driven convection.

31   The sediment load in a river can be estimated by using a rating curve for the sediment load as a

1   function of river flow rate (Q). Hence, it is possible to estimate the density ratio (R_ρ) as a

2   function of Q for a river flowing into a salty ocean. Equation (11) can then be used to predict the

3   length-scale over which sedimentation could occur, as was done in the example of the Squamish

4   River. In these oceanic cases it is reasonable to ignore temperature effects, as large salinity

5   differences dominate the density differences. To make the same estimates using Equation (11)

6   for a lake, it would also require that the temperature of the river and the seasonal thermal

7   stratification of the lake be known. For example, Cossu *et al*. (2015) discussed how the

8   seasonality in sediment loading in rivers and changes of the thermal stratification in an alpine

9   lake could greatly influence whether overflows, interflows or underflows occurred. Hopefully,

10   future research into these processes will include measurements of the density ratio, and the

11   design of field observations can be guided by the predictions of Equation (11) and the time-lapse

12   movies contained in the Supplemental section.

13

18

19

1   **NOMENCLATURE**

2

3   a Empirical rating coefficient

4   b Empirical rating coefficient

5   C Average concentration of the flow (kg m^{-3})

6   C_s Concentration of suspended sediment (kg m^{-3})

7    $C_{s\,Average}$ Average concentration of suspended sediment (kg m^{-3})

8    $C_{s\,Flood}$ Concentration of suspended sediment during a flood (kg m^{-3})

9   c_t Dimensionless multiple of time that takes for settling-driven convection to

10   develop

11   C_0 Initial concentration of the flow (kg m^{-3})

12   c_1 1st dimensional constant (m s^{-1})

13   c_{1avg} Average value of the 1st dimensional constants (m s^{-1})

14   c_2 2nd dimensional constant (s)

15   c_{2avg} Average value of the 2nd dimensional constants (s)

16   Fr   Froude number

17   g Gravitational acceleration (9.81 m s^{-2})

18   g' Reduced gravity (m s^{-2})

19   g'_C Reduced gravity in terms of density difference due to the added sediment (m s^{-2})

20   Gr   Grashof number

21   H Thickness of the current (m)

22   $\bar{H}$ Mean thickness of the current (m)

23   L_C Thickness of the nose region (m)

24   L_{prop} Propagation length-scale of the current (m)

25   m_C Mass of sediment particles (kg)

26   m_{comp} Mass of the water in the small compartment (kg)

27   Q The flow rate of a river (m^3 s^{-1})

28   $Q_{Average}$ Average flow rate of a river (m^3 s^{-1})

29   Q_{Flood} Flow rate of a river during flood (m^3 s^{-1})

30   Re   Reynolds number

31   R_ρ Density ratio

1   **NOMENCLATURE CONTINUED**

2

3   T_S Settling time-scale of sediment particles (s)

4   t Time (s)

5   t_{comp} Temperature of the small compartment (°C)

6   t_S Temperature of the saline ambient (°C)

7   t_0 Time corresponding to the initial stable density profile (s)

8   U Horizontal velocity of the current (m s^{-1})

9   V_{comp} Volume of the compartment (m^3)

10   w Vertical velocity of the fluid in the nose region (m s^{-1})

11   w_S Stokes settling velocity of sediment particles (m s^{-1})

12   $\Delta\rho$ Density difference between the current and the saline ambient (kg m^{-3})

13   $\Delta\rho_C$ Density differences due to the added sediment (kg m^{-3})

14   $\Delta\rho_S$ Density differences due to the added salt (kg m^{-3})

15   $\Delta\rho_{SeaWater}$ Density difference due to the added salt for sea water at 15 °C

16   Δt Elapsed time between the stable and the unstable density profiles (s)

17   φ Mass concentration of sediment particles (kg kg^{-1})

18   γ Density expansion coefficient for SiC particles

19   v Coefficient of kinematic viscosity of fresh water at 20 °C (10^{-6} m^2 s^{-1})

20   ρ Average density between the current and the saline ambient (kg m^{-3})

21   ρ_C Density of the sediment-laden water (kg m^{-3})

22   ρ_{comp} Density of the small compartment before adding sediment (kg m^{-3})

23   ρ_f Total density of a fluid (kg m^{-3})

24   ρ_S Density of the saline ambient (kg m^{-3})

25   ρ_{SiC} Density of SiC particles (3210 kg m^{-3})

26   ρ_0 Density of clear fresh water at 20°C (998.2 kg m^{-3})

27

28

1   **REFERENCES**
2
3   **Ayranci, K., Lintern, D.G., Hill, P.R**. and **Dashtgard, S.E.** (2012) Tide-supported gravity
4   flows on the upper delta front, Fraser River delta, Canada. *Mar. Geol.*, **326**, 166 – 170.
5
6   **Benjamin, T.B.** (1968) Gravity currents and related phenomena. *J. Fluid Mech.*, **31**, 209 – 248.
7
8   **Burns, P.** and **Meiburg, E.** (2012) Sediment-laden fresh water above salt water: Linear stability
9   analysis. *J. Fluid Mech.*, **691**, 279 – 314.
10
11   **Burns, P.** and **Meiburg, E.** (2015) Sediment-laden fresh water above salt water: Nonlinear
12   stability analysis. *J. Fluid Mech.*, **762**, 156 – 195.
13
14   **Carazzo, G.** and **Jellinek, A.M.** (2012) A new view of the dynamics, stability and longevity of
15   volcanic clouds. *Earth Planet. Sci. Lett.*, **325 – 326**, 39 – 51.
16
17   **Carazzo, G.** and **Jellinek, A.M.** (2013) Particle sedimentation and diffusive convection in
18   volcanic ash-clouds. *J. Geophys. Res. Solid Earth*, **18**, 1420 – 1437, doi:10.1002/jgrb.50155.
19
20   **Chen, C.F.** (1997) Particle flux through sediment fingers. *Deep Sea Res.*, **44** (9 – 10), 1645 –
21   1654.
22
23   **Clare, M.A., Clarke, J.H., Talling, P.J., Cartigny, M.J.B.** and **Pratomo, D.G.** (2016)
24   Preconditioning and triggering of offshore slope failures and turbidity currents revealed by most
25   detailed monitoring yet at a fjord-head delta. *Earth Planet. Sci. Lett.*, **450**, 208 – 220.
26
27   **Cossu, R., Forrest A.L., Roop, H.A., Dunbar, G.B., Vandergoes, M.J., Levy, R.H.,**
28   **Stumoner, P.** and **Schladow, S. G.** (2015) Seasonal variability in turbidity currents in Lake
29   Ohau, New Zealand, and their influence on sedimentation. *Mar. Freshwater Res.*,
30   doi:10.1071/MF15043.
31
32   **Davarpanah Jazi, S.** and **Wells, M.G.** (2016) Enhanced sedimentation beneath particle-laden
33   flows in lakes and the ocean due to double-diffusive convection. *Geophys. Res. Lett.*, **43** (20),
34   10883 – 10890, doi: 10.1002/2016GL069547.
35
36   **Forel, F.A.** (1885) Les ravins sous-lacustres des fleuves glaciaires. Comptes Rendus de
37   l'Académie des Sciences de Paris: 1-3.
38
39   **Geyer, W.R., Hill, P.S.** and **Kineke, G.C.** (2004) The transport, transformation and dispersal of
40   sediment by buoyant coastal flows. *Cont. Shelf Res.*, **1212** (24), 927 – 949.
41
42   **Gilbert, R.** and **Butler, R.D.** (2004) The physical limnology and sedimentology of Meziadin
43   Lake, northern British Columbia, Canada. *Arct. Antarct. Alp. Res.*, **36** (1), 33 – 41.
44

Giovanoli, F. (1990) Horizontal transport and sedimentation by interflows and turbidity currents in Lake Geneva. In *Large Lakes*, edited by Tilzer, M. M. and Serruya, C., pp. 175 – 195, Springer, Berlin.

Gladstone, C. and **Pritchard, D.** (2010) Patterns of deposition from experimental turbidity currents with reversing buoyancy. *Sedimentology*, **57**, 53 – 84.

Green, T. (1987) The importance of double diffusion to the settling of suspended material. *Sedimentology*, **34**, 319 – 331.

Hill, P.S., Milligan, T.G. and **Geyer, W.R.** (2000) Controls on effective settling velocity of suspended sediment in the Eel River flood plume, *Cont. Shelf Res.*, **20** (16), 2095 – 2111.

Hill, P.R., Conway, K., Lintern, D.G., Meulé, S., Picard, K. and **Barrie, J.V.** (2008) Sedimentary processes and sediment dispersal in the southern Strait of Georgia, BC, Canada. *Mar. Environ. Res.*, **66**, S39 – S48.

Hizzett, J.L., Hughes Clarke, J.E., Sumner, E.J., Cartigny, M.J.B., Talling, P. J. and **Clare, M.A.** (2017) Which triggers produce the most erosive, frequent and longest runout turbidity currents on deltas? *Geophys. Res. Lett.*, **45**, doi: 10.1002/2017GL075751.

Horner-Devine, A.R., Hetland, R.D. and **MacDonald, D.G.** (2015) Mixing and transport in coastal river plumes. *Annu. Rev. Fluid Mech.*, **47**, 569 – 594.

Houk, D. and **Green, T.** (1973) Descent rates of suspension fingers. *Deep Sea Res.*, **20**, 757 – 761.

Hoyal, D.C.J.D., Bursik, M.I. and **Atkinson, J.F.** (1999a) The influence of diffusive convection on sedimentation from buoyant plumes. *Mar. Geol.*, **159**, 205 – 220.

Hoyal, D.C.J.D., Bursik, M.I. and **Atkinson, J.F.** (1999b) Settling-driven convection: A mechanism of sedimentation from stratified fluids. *J. Geophys. Res.*, **104** (C4), 7953 – 7966, doi: 10.1029/1998JC900065.

Huppert, H.E. (2006) Gravity currents: a personal perspective. *J. Fluid Mech.*, **554**, 299 – 322.

Hughes Clarke, J.E., Marques, C.R.V. and **Pratomo, D.** (2014) Imaging active mass-wasting and sediment flows on a fjord delta, Squamish, British Columbia. In *Submarine Mass Movements and Their Consequences*, 249 – 260, Springer.

Kineke, G. C., Woolfe, K. J., Kuehl, S. A., Milliman, J. D., Dellapenna, T. M. and **Purdon, R. G.** (2000) Sediment export from the Sepik River, Papua New Guinea: evidence for a divergent sediment plume. *Cont. Shelf Res.*, **20** (16), 2239 – 2266.

Lintern, D. G., Hill, P. R. and **Stacey, C.** (2016) Powerful unconfined turbidity current captured by cabled observatory on the Fraser River delta slope, British Columbia, Canada. *Sedimentology*,

63 (5), 1041 – 1064.

Manzella, I., Bonadonna, C., Phillips, J.C. and **Monnard, H.** (2015) The role of gravitational instabilities in deposition of volcanic ash. *Geology*, **43** (3), 211 – 214.

Martin, D. and **Nokes, R.** (1998) Crystal settling in a vigorously convecting magma chamber. *Nature*, **332**,534 – 536.

Maxworthy, T. (1999) The dynamics of sedimenting surface gravity currents. *J. Fluid Mech.*, **392**, 27 – 44.

Meiburg, E. and **Kneller, B.C.** (2010) Turbidity currents and their deposits. *Annu. Rev. Fluid Mech.*, **42**, 135 – 156.

Mulder, T. and **Chapron, E.** (2011) Flood deposits in continental and marine environments: character and significance. In *Sediment Transport from Shelf to Deep Water — Revisiting the Delivery System*, AAPG Stud. Geol., vol. **61**, edited by R. M. Slatt and C. Zavala, pp. 1 – 30.

Mulder, T. and **Syvitski, J.P.M.** (1995) Turbidity currents generated at river mouths during exceptional discharges to the world oceans. *J. Geol.*, **103** (3), 285 – 299.

Nowacki, D.J., Horner-Devine, A.R., Nash, J.D. and **Jay, D.A.** (2012) Rapid sediment removal from the Columbia River plume nearfield. *Cont. Shelf Res.* **35**, 16 – 28.

Parsons, J.D. and **Garcia, M.H.** (2000) Enhanced sediment scavenging due to double-diffusive convection. *J. Sediment. Res.*, **70** (1), 47 – 52.

Parsons, J.D., Bush, J.W.M. and **Syvitski, J.P.M.** (2001) Hyperpycnal plume formation from riverine outflows with small sediment concentrations. *Sedimentology*, **48** (2), 465 – 478.

Penney, J. and **Stastna, M.** (2016) Direct numerical simulation of double-diffusive gravity currents. Physics of Fluids **28**, 086602; doi: 10.1063/1.4961045.

Rouhnia, M. and **Strom, K.** (2015) Sedimentation from flocculated suspensions in the presence of settling-driven gravitational interface instabilities. *J. Geophys. Res. Oceans*, **120**, 6384 – 6404, doi: 10.1002/2015JC010750.

Rouhnia, M. and **Strom, K.** (2017) Sedimentation from buoyant muddy plumes in the presence of interface mixing: an experimental study. *J. Geophys. Res. Oceans*, **120**, 2652 – 2670, doi: 10.1002/2016JC012053.

Shao, Y.C., Hung, C.Y. and **Chou, Y.J.** (2017) Numerical study of convective sedimentation through a sharp density interface. *J. Fluid Mech.,* **824**, 513 - 549.

Scheu, K.R., Fong, D.A., Monismith, S.G. and **Fringer, O.B.** (2015) Sediment transport dynamics near a river inflow in a large alpine lake. *Limnol. Oceanogr.*, **60** (4), 1195 – 1211.

Simpson, J.E. (1982) Gravity currents in the laboratory, atmosphere and ocean. *Ann. Rev. Fluid Mech.*, **14** (1), 213 – 234.

Snow, K. and **Sutherland, B.R.** (2014) Particle-laden flow down a slope in uniform stratification. *J. Fluid Mech.*, **755**, 251 – 273.

Scollo, S., Bonadonna, C., and **Manzella, I.** (2017) Settling-driven gravitational instabilities associated with volcanic clouds: new insights from experimental investigations. *Bulletin of Volcanology*, **79**:39. https://doi.org/10.1007/s00445-017-1124-x.

Sparks, R.S.J., Carey, S.N. and **Sigurdsson, H.** (1991). Sedimentation from gravity currents generated by turbulent plumes. *Sedimentology*, **38** (5), 839 - 856.

Stack, K. M., Grotzinger, J. P., Lamb, M. P., Gupta, S., Rubin, D. M., Kah, L. C., Edgar, L. A., Fey, D. M., Hurowitz, J. A., McBride, M., Rivera-Hernández, F., Sumner, D. Y., Van Beek, J. K., Williams, R. M. E., and **Yingst, R. A.** (2018) Evidence for plunging river plume deposits in the Pahrump Hills member of the Murray formation, Gale crater, Mars. *Sedimentology,* doi: 10.1111/sed.12558

Sutherland, B.R., Gingras, M.K., Knudson, C., Steverango, L. and **Surma, C.** (2018) Particle-bearing currents in uniform density and two-layer fluids. *Phy. Rev. Fluids*, 3 (2), p.023801.

Talling, P. J., Paull, C.K. and **Piper, D.J.W.** (2013) How are subaqueous sediment density flows triggered, what is their internal structure and how does it evolve? Direct observations from monitoring of active flows. *Earth-Sci. Rev.*, **112**, 244 - 288.

Turner, J. S. (1979) Buoyancy Effects in Fluids. Cambridge University Press.

Warrick, J. A., Xu, J., Marlene, A. N. and **Homa, J. L.** (2008) Rapid formation of hyperpycnal sediment gravity currents offshore of a semi-arid California river. *Cont. Shelf Res.*, **28**, 991 – 1009.

Yuan, Y. and **Horner-Devine, A.R.** (2017) Experimental investigation of large-scale vortices in a freely spreading gravity current. *Phys. Fluids*, 29(10), p.106603. https://doi.org/10.1063/1.5006176.

Yu, X., Hsu, T. J. and **Balachandar, S.** (2013) Convective instability in sedimentation: Linear stability analysis. *J. Geophys. Res. Oceans*, **118**, 256 – 272, doi:10.1029/2012JC008255.

Yu, X., Hsu, T. J. and **Balachandar, S.** (2014) Convective instability in sedimentation: 3-D numerical study. *J. Geophys. Res. Oceans*, **119**, 8141 – 8161, doi:10.1002/2014JC010123.

Zhixin, Q., Eames, I. and **Greig, A.** (2014) Flushing ballast tanks. *Ocean Eng.*, **89**, 157 – 172.

Dynamics of settling-driven convection beneath a sediment-laden buoyant overflow: implications for the length-scale of deposition in lakes and the coastal ocean

Shahrzad Davarpanah Jazi and Mathew G. Wells

Department of Physical & Environmental Sciences, University of Toronto
1065 Military Trail, M1C 1A4, Toronto, ON, Canada
Email: sh.davarpanahjazi@mail.utoronto.ca, Email: wells@utsc.utoronto.ca

ABSTRACT

A series of laboratory experiments were conducted in order to determine how settling-driven convection influences the length-scale over which the majority of particles settle beneath a buoyant sediment-laden plume spreading over a denser saline layer. This system is analogous to sediment-laden river water spreading into a lake or the coastal ocean. The key dimensionless parameter that controls the settling dynamics of such flows is the density ratio, defined as the ratio of density differences due to the added salt and sediment. For a buoyant plume, this ratio has to be greater than unity, so that the experiments in the current study were performed for density ratios between one and five. When density ratio was close to one, settling-driven convection was vigorous and the length-scale over which sedimentation occurred was very small. A strong secondary turbidity current was generated in this case. On the other hand, for larger values of density ratio, the predicted length-scale over which a secondary plume was generated increased proportional with the density ratio. A complete mathematical expression for this length-scale was developed using recent theory that described the time-scale over which settling-driven convection evolved. The theoretically predicted propagation length-scale showed very good quantitative agreement with laboratory experiments. The use of the dimensionless density ratio allows the expression to predict which sediment-laden river plumes in lakes and the coastal ocean could quickly form secondary turbidity currents.

Keywords: Sediment-laden gravity current, settling-driven convection, turbidity currents, density ratio, Stokes settling velocity, overflow.

INTRODUCTION

Rivers are the main pathways by which sediment is transported to the coastal regions of lakes and the ocean (Mulder & Syvitski, 1995). In a lake, a sediment-laden river is often denser than the receiving waters and so can readily plunge and form a turbidity current, as originally observed in pioneering work by Forel (1885) in Lake Geneva. In contrast, when a river flows into the coastal ocean, the buoyant density difference between the fresh and saline water is usually far greater than the unstable density difference due to the suspended sediment load. Hence, almost all sediment-laden rivers will form surface plumes in the coastal ocean (Mulder & Syvitski, 1995). The processes that control the length-scale over which sediment deposits beneath these buoyant sediment-laden plumes is thus a key geological question. This length-scale of deposition is directly related to the length-scale that the buoyant plume propagates before losing all its sediment from beneath. Such length-scale has been described as the product of the horizontal velocity of the buoyant plume and a time-scale over which sediment is lost (Geyer *et al.*, 2004; Hill *et al.*, 2000). The horizontal ~~velocities~~ velocity of a surface plume is well understood (Yuan & Horner-Devine, 2017), and in the absence of strong winds or tides, it is largely determined by buoyancy forces (Horner-Devine ~~at~~ *et al.*, 2015). The time-scale over which sedimentation occurs has been the focus of recent work by Hoyal *et al.* (1999b), Burns & Meiburg (2012, 2015) and Davarpanah Jazi & Wells (2016), who identified settling-driven convection as the potentially dominant fluid dynamical process that can rapidly transport sediment from beneath sediment-laden buoyant plumes. Previous experiments ~~on buoyant surface sediment-laden plumes~~ (Maxworthy, 1999; Parsons *et al.*, 2001; Snow & Sutherland, 2014; Sutherland *et al.,* 2018) and direct observations of buoyant surface sediment-laden plumes (Hughes Clarke *et al.*, 2014; Hizzett *et al.*, 2017) ~~have shown~~ showed that under certain conditions, the rapid sediment loss beneath such plumes can generate a secondary turbidity current, which could provide an important mechanism to transport sediment to the depths of the ocean from the continental margin. For instance, direct field monitoring by Clare *et al.* (2016) has revealed that 70% of observations of the triggering of secondary turbidity currents were linked to the sediment-laden plume in Howe Sound near the Squamish River in BC, Canada. Since sediment-laden gravity currents are one of the main mechanisms for transporting ~~sediment~~ sediments into the deep ocean, where deep sand layers can form (Meiburg & Kneller, 2010), this

study aims to use laboratory experiments to quantify the conditions that can enhance sedimentation beneath such buoyant river plumes. Particularly, this study identifies the specific conditions that could potentially result in the formation of secondary turbidity currents from the many rivers in the coastal ocean that usually have low sediment loads and would almost always form surface plumes rather than plunging hyperpycnal underflows (Mulder & Syvitski, 1995).

The length-scale over which a surface plume propagates and loses sediment will give a first-order estimate of the distribution of sediment deposition from a river mouth, as illustrated schematically in Figure 1. If there are no currents beneath the surface plume, then the distance at which all of the sediment has fallen out of the plume determines the zone of deposition. If the concentrations are high enough, this depositing sediment could also potentially form a secondary turbidity current. Intuitively, the extent of propagation over which sediment is lost (L_{prop}) can be approximated with equation (1) as follows:

$$L_{prop} = U\,T_s = U(\overline{H}/w_S) \tag{1}$$

where U is the horizontal velocity of the buoyant plume and T_S is the time-scale over which particles settle through the moving surface plume. If particles are only being lost by a slow settling rate over the mean thickness of the plume ($\overline{H}$), then the settling time-scale is simply determined as $T_S = \overline{H} / w_S$, where w_S is the Stokes settling velocity of the sediment particles (Geyer $et\ al.$, 2004; Hill $et\ al.$, 2000). The horizontal velocity of a buoyant plume (U) is a function of the reduced gravity (g') between the plume and ambient and the thickness at the plume head (H). Thus, this velocity is given by $U = $ Fr $(g'H)^{1/2}$, where the reduced gravity is defined as $g' = g\,\Delta\rho\,/\,\rho$, with g the gravitational acceleration (9.81 m s^{-2}) and $\Delta\rho$ and ρ are respectively the density difference and average density between the current and the saline ambient with units of kg m^{-3}. The Froude number is the key dimensionless parameter for describing gravity current dynamics and is defined as Fr $= U\,/\,(g'H)^{1/2}$. Essentially the Froude number compares the observed speed to that of an internal wave speed. Numerous experimental studies have consistently found the Froude number to be order one (i.e. Turner, 1979; Simpson, 1982; Gladstone & Pritchard, 2010; Snow & Sutherland, 2014), which is close to the value of 1 / $\sqrt{2}$ found in theoretical studies (Benjamin, 1968; Huppert, 2006; Meiburg & Kneller, 2010).

4

Recent direct numerical simulations of buoyant double-diffusive gravity currents by Penney & Stastna (2016) have suggested that a no-slip condition (representing a solid lid) may increase drag compared to a free-slip condition (representing an air-water interface), and hence they would predict different Fr than for buoyant plumes compared to regular bottom gravity currents.

Using typical values for lab laboratory and field situations, Equation (1) predicts very large propagation length-scales if the only settling process considered is Stokes settling velocity. For instance a typical gravity current in a lab laboratory experiment with a strong buoyancy difference, has a speed of order $U \sim 0.1$ m s^{-1}. The mean thickness of a typical laboratory gravity current is of order $\overline{H} = 0.1$ m. Hence, using for example Silicon Carbide (SiC) sediment particles of size 7.8×10^{-6} m with Stokes settling velocity of $w_S = 7.7 \times 10^{-5}$ m s^{-1}, implies a settling time of $T_S = 1300$ s. Therefore, assuming that the current is moving at 0.1 m s^{-1}, it would need to propagate the very large distance of 130 m for all the particles to settle out of the plume, and hence laboratory plumes with fine sediment might be predicted to propagate to the end of any realistic experimental tank before losing all of their sediment. In contrast, previous laboratory experiments have found that settling-driven convection is much more important than just the Stokes settling velocity, so that laboratory plumes with fine sediment particles can lose sediment at much faster rates (Maxworthy, 1999; Parsons *et al.*, 2001; Snow & Sutherland, 2014, Sutherland *et al.*, 2018). The scaling in Equation (1) assumes that within the gravity current particles are settling in a laminar fashion manner within the gravity current. If the flow is turbulent however, so that the concentration is well mixed, then the average mass concentration (C with units of kg m^{-3}) in the flow changes with time as $C(t) = C_o e^{(-t W_s / \overline{H})}$ (Martin & Nokes, 1988; Sparks *et al.*, 1991), where C_0 is the initial mass concentration of the flow (kg m^{-3}). With such an exponential decay, 95% of particles settle out after 3 three settling time-scales, i.e. an even greater distance is implied by Equation (1).

There are a number of mechanisms by which the time-scale used in Equation (1) could be much smaller than that predicted from the Stokes settling velocity of a single particle, including flocculation (Rouhnia & Strom, 2015, 2017) and settling-driven convection (Burns & Meiburg, 2012, 2015). This study will focus on the potential role of settling-driven convection, as the description of increased settling rates due to flocculation is now quite mature (Rouhnia & Strom,

2015, 2017). Several field observations have found that sediment is lost from a buoyant plume at rates much faster than predicted by the Stokes settling velocity. For instance, Nowacki *et al.* (2012) computed the sediment removal rate from the Colombia River, USA and determined that the settling rate (10 mm s^{-1}) was substantially larger than the settling velocity of a single particle (2 mm s^{-1}). Similarly, Scheu *et al.*, (2015) used acoustic backscatter measurements beneath a river plume in a thermally stratified lake, to infer increases of an order of magnitude over the Stokes settling velocities of the suspended sediments settling from turbid river plumes. In the absence of flocculation, the most likely potential mechanism for these increased sedimentation rates is settling-driven convection, the vigour of which depends upon the unstable sediment contrast between the layers.

Settling-driven convection is an important instability that can occur when a layer of fresh sediment-laden water lies above a layer of saline water (Fig. 2). Initially this configuration can be stable if the mean density of the upper layer is less than that of the lower layer (as shown in Figure 2A). However, as sediment settles through the saline interface, a layer of particle rich fluid forms that contains both salt and sediment, and is now denser than the fluid below (the nose region in Figure 2B). Since this layer is unstable, convection of sediment-laden plumes begins (Fig. 2C). These dense sediment-laden finger-like plumes sink with vertical velocities that are 10 to 100 times larger than Stokes settling velocity (Hoyal *et al.*, 1999b; Burns & Meiburg, 2012, 2015; Davarpanah Jazi & Wells, 2016). This process is highly important to Equation (1), as it suggests that a much shorter time-scale T_s is relevant for sediment-laden buoyant plumes, so that the deposition length-scale will be far less than predicted by only assuming Stokes settling velocity of a single particle. Such finger-like plumes have been seen in a number of studies (Bradly, 1965; Hoyal *et al.*, 1999b) and this process is seen to greatly increase the particle removal rate from an otherwise buoyant upper layer (Houk & Green, 1973; Green, 1987; Chen, 1997; Hoyal *et al.*, 1999a, b; Maxworthy, 1999; Parsons & Garcia, 2000; Parsons *et al.*, 2001; Davarpanah Jazi & Wells, 2016). Recent work by Davarpanah Jazi & Wells (2016) found showed that in a salt/sediment configuration with no horizontal velocities, the vigour of convection was dictated by density ratio defined as $R_\rho = \Delta\rho_S / \Delta\rho_C$, the ratio of density differences due to the added salt ($\Delta\rho_S$) and sediment ($\Delta\rho_C$). For a sediment-laden layer of fresh water to float above a saline layer, R_ρ must be greater than one. The most vigorous convection

was found to occur for marginal stability when R_ρ was very close to one. Theoretical and numerical ~~descriptions~~ studies of settling-driven convection (Burns & Meiburg, 2012, 2015; Yu *et al.*, 2013, 2014; Shao *et al.*, 2017) have quantified the time-scales for these processes, and revealed the internal dynamics of the velocity fields that are difficult to see experimentally.

One of the key findings of the previous experiments and field observations on buoyant sediment-laden plumes is that settling-driven convection is an important mechanism for moving sediments rapidly from surface plumes to the lake or ocean bed, where dense secondary turbidity currents can potentially form (Maxworthy, 1999; Parsons *et al.*, 2001; Snow & Sutherland, 2014; Hughes Clarke *et al.*, 2014; Sutherland *et al.*, 2018). As almost all sediment-laden river plumes are initially buoyant, ~~over a hundred~~ many papers have cited Parsons *et al.* (2001) to suggest settling-driven convection could be a key process by which turbidity currents can be formed in the coastal ocean near river mouths, which ultimately transport sediment to deep regions of the ocean (Meiburg & Kneller, 2010). It is very challenging in a field study to isolate the specific mechanism by which secondary turbidity currents can be generated from a buoyant sediment-laden plume (Gales et al., 2018), and only a limited number of field studies have attempted to investigate this process (see for example optical backscatter measurements of Hughes Clarke *et al.* 2014, Kineke *et al.* 2000 and Hill *et al.* 2008). This has placed great importance to these earlier experiments, especially Parsons *et al.* (2001). In the current study, the aim is to revisit these earlier experiments, and improve the understanding on processes that set the length-scale in Equation (1) in light of the recent improvements to the theoretical understanding of the time-scales of settling-driven convection (Burns & Meiburg, 2012, 2015; Yu *et al.*, 2013, 2014; Shao *et al.*, 2017). Specifically, this paper aims to extend the initial study of Maxworthy (1999) by applying the time-scale used in Burns & Meiburg (2012, 2015) to determine how the length-scale in Equation (1) varies as a function of density ratio (R_ρ).

The experiments in this paper aim to quantify how settling-driven convection could control the length-scale of deposition beneath a buoyant plume, and isolate the specific conditions under which secondary turbidity currents can form. As this process is challenging to study in the field, the presented experimental visualizations of such processes will help geologists to better conceptualize field observations. Using the most recent results from modelling of settling-driven

convection, a new equation is developed to describe the distance over which sediment is lost due to settling-driven convection. There is excellent agreement between the quantitative theory and the laboratory results. The paper ends with an extrapolation of the findings of this study to predict the relevant length-scales for river plumes entering the coastal ocean.

EXPERIMENTAL DESIGN

In order to better understand how the process of settling-driven convection controls deposition beneath buoyant plumes in lakes and the coastal ocean, a series of experiments were performed, where a controlled volume of sediment-laden fluid was released into a large tank that contained a well-mixed saline solution (Fig. 3). The large tank had dimensions of 1.83 × 0.55 × 0.305 m, and sediment-laden fluid was initially contained behind a removable metal barrier in a compartment of dimensions 0.35 × 0.115 × 0.23 m. The two compartments were the same temperature, as they were both filled with tap water stored in large vessels that had equilibrated with room temperature (18.5 ± 2.3 °C). Keeping the temperature constant throughout all experiments, resulted in a two-component salt/sediment configuration similar to experiments of Maxworthy (1999). The ambient saline solution was prepared from high purity food grade salt. The sediment used in the experiments was Silicon Carbide (SiC) grinding powder with a density of ρ_{SiC} = 3210 kg m^{-3}. This material is monodispersed and non-cohesive and was previously used in the experiments of Maxworthy (1999), Hoyal *et al.* (1999b), Davarpanah Jazi & Wells (2016) and Sutherland *et al.* 2018. The median diameter of particles was 7.8 × 10^{-6} m, resulting in a predicted Stokes settling velocity of 7.7 × 10^{-5} m s^{-1}.

In these experiments, the salinity contrast between the surface plume and the ambient fluid was kept constant, and the sediment concentration was increased. Thus, the density ratios varied from R_ρ = ∞ (no sediment) to R_ρ = 1 (neutral stability). The cases where R_ρ < 1 would have the sediment being denser than the ambient fluid so would immediately form underflows. The density of the saline ambient (ρ_S) was kept constant at 1002.5 ± 0.4 kg/m^3, while the amount of sediment added to surface plume was varied. The different densities of sediment-laden water (ρ_C) were obtained by adding various masses of sediment ($0 \leq m_C \leq 0.065$ kg) to the fixed volume of fresh water within the small compartment. The mass of sediment was determined using an Ohaus

SPX222 balance (Ohaus Corporation, Parsippany, NJ, USA) with precision of 10^{-2} g. The densities of saline water (ρ_S) and the water in the compartment, before adding sediment (ρ_{comp}), were measured using an Anton Paar DMA 35 Ex portable densitometer (Anton Paar USA Inc., Ashland, VA, USA) with an accuracy of $\pm$ 10^{-3} g cm^{-3} and a resolution to 10^{-4} g cm^{-3}. The temperatures (t_S and t_{comp}) were measured simultaneously with the same instrument to the precision of 0.2 °C.

The density of a fluid can be determined as $\rho_f = \rho_0 + \Delta\rho_S + \Delta\rho_C$ and is linearly related to both concentrations of salt and sediment. Here, ρ_0 is the density of clear fresh water at 20°C (998.2 kg m^{-3}). The added density due to the added salt was calculated using $\Delta\rho_S = \rho_S - \rho_{comp}$, where the density of fresh water in the compartment is $\rho_{comp} = 999.1 \pm 0.2$ kg m^{-3}. The density anomaly due to the added sediment was calculated as $\Delta\rho_C = \gamma\,C\,\rho_{comp}$, in which γ is the density expansion coefficient for SiC particles defined as ($\rho_{SiC} - \rho_{comp}$) / ρ_{SiC}. Furthermore, φ is the mass concentration of sediment particles (kg kg^{-1}) denoted by $\varphi = m_C / (m_C + m_{comp})$, where the mass of the water in the small compartment (m_{comp}) was determined as $m_{comp} = \rho_{comp}\,V_{comp}$, in which V_{comp} was the volume of the compartment (m^3).

The entire tank was initially filled with saline water with density ρ_S, and then the barrier was inserted to isolate the smaller compartment. With the use of two small pumps, the saline water in this compartment was replaced with freshwater, by discharging salt water out and pumping fresh water in simultaneously. An equivalent of four times the volume of the small compartment was replaced in order to guarantee that 99% of the saline water was flushed out (Zhixin *et al.*, 2014). An electrical mixer was used to keep the fluid well-mixed while being replaced.

The sediment particles were then added to the fresh water in the small compartment and a well-mixed constant volume of sediment-laden water was prepared. The electrical mixer kept the fluid stirred to inhibit the settling of particles and the total time between addition of sediment and removal of barrier was kept to less than two minutes. Each experiment commenced with the gentle removal of the metal barrier 10 s after the mixer was turned off to prevent turbulent motion it produced within the fluid. In addition, food dye was added to the sediment water to further improve flow detection. Digital cameras were used to capture the behaviour of the flow

from different angles through photos and movies. Two large LED light panels provided bright and uniform lighting at the background in order to produce clear, sharp photos and movies from the sediment-laden gravity current in motion.

A total of 19 experiments with density ratios in the range of $0.687 \leq R_\rho \leq \infty$ were performed. Full details of all 19 experiments, including R_ρ, m_C, L_{prop} and the behaviour of sediment-laden overflows, are summarized in Table 1. The six supplemental movies are available online and are representative of the major trends in the behaviour of the current. In this table the experiments are in an ascending order based on their density ratio. The experiment with $R_\rho = \infty$ (Movie S6 in the Supplemental section) had no sediment, and the one experiment with $R_\rho = 0.687$ (Movie S1 in the Supplemental section) had sediment load such that it was initially denser than saline ambient; all the other 17 experiments were initially positively buoyant and were in the range $1.021 \leq R_\rho \leq 4.575$. The above two experiments ($R_\rho = \infty$ and 0.687) were performed only for comparison purposes, as the main focus of this study was on ~~particle-laden~~ sediment-laden overflows. The propagation length-scale of the gravity current (L_{prop}) was measured by visually determining the distance at which the thickness of the gravity current became less than 0.01 m and had essentially stopped. The error bars in the determinations of L_{prop} represent an estimate of the distance over which the gravity current changes from 0.02 m to 0 m thickness.

THEORY

Settling-driven convection can lead to far greater loss of sediments than Stokes settling, so that use of Equation (1) would predict a much smaller and more realistic deposition length-scale. In this section, the scaling of L_{prop} is now modified to take into account theoretical scaling of the sedimentation time-scale, introduced by Burns & Meiburg (2012, 2015) to show how the density ratio (R_ρ) and the stratification influence the propagation length-scale. In order to use Equation (1) a horizontal velocity (U) and a sedimentation time-scale (T_S) are needed. For the former, the horizontal velocity of the plume is a function of the reduced gravity, which can be expressed in terms of the contribution of sediment and salt density anomalies as,

$$U = \mathrm{Fr}\,\left(\frac{g\,H}{\rho}\,(-\Delta\rho_C + \Delta\rho_S)\right)^{1/2} \qquad (2)$$

where $\Delta\rho_S$ and $\Delta\rho_C$ are the added density due to the added salt and mass fraction of sediment respectively. By introducing the definition of density ratio ($R_\rho = \Delta\rho_S / \Delta\rho_C$) previously used by Davarpanah Jazi & Wells (2016), this velocity can be rewritten in terms of density ratio (R_ρ) and Froude number (Fr) as,

$$U = \text{Fr}\left(\frac{g\,\Delta\rho_S}{\rho}H\left(1 - \frac{1}{R_\rho}\right)\right)^{1/2} \tag{3}$$

The sedimentation time-scale (T_S) is determined by the dynamics of the instability at the interface between sediment-laden and saline fluid (Burns & Meiburg, 2015). The downward settling of sediment particles from the fresher layer into the denser saline layer (Fig. 2A) drives the settling-driven convection instability. A very thin layer of fluid, just below the interface containing both salt and sediment, forms a "nose" of unstable stratification with length-scale (L_C), as shown in Figure 2B. The convective instability at the base of the sediment-laden fluid is controlled by this thin "nose" region, as there is an unstable density inversion due to accumulation of settling sediment from above (Burns & Meiburg, 2012). When this layer grows sufficiently large, the dense material will sink as a convective plume (Fig. 2C). The numerical simulations of Burns & Meiburg (2012, 2015) and Shao *et al.* (2017) have shown that within the thin nose region of thickness L_C, the fluid dynamics are dominated by viscosity. This implies that both Grashof number and Reynolds number are equal to one at the point just before instability occurs.

The Grashof number is defined as,

$$Gr = \frac{g'_C\,L_C^3}{v^2} \tag{4}$$

where $g'_C = g\,\Delta\rho_C / \rho_0$ is the reduced gravity defined in terms of the density difference due to the added sediment ($\Delta\rho_C$) and density of fresh water (ρ_0) (Burns & Meiburg, 2012, 2015) and $v = 10^{-6}$ m^2 s^{-1} is the coefficient of kinematic viscosity of fresh water at 20 $^{\circ}$C. In this region, a Reynolds number can also be defined as,

$$\mathrm{Re} = \frac{w_S L_C}{v} \tag{5}$$

where the vertical velocity of fluid in this layer is assumed to be the same as the settling velocity w_s (Shao *et al.*, 2017).

The important time-scale for convective instability can be derived through the following steps. First, assuming Re = 1 implies that

$$L_C \equiv \frac{v}{w_S} \tag{6}$$

Similarly assuming that in the viscosity dominated unstable nose region Gr = 1 results in a scaling for the thickness of the nose region in terms of the viscosity and reduced gravity as,

$$L_C \equiv \left(\frac{v^2}{g_C'}\right)^{1/3} \tag{7}$$

Note that g_C' is the reduced gravity defined in terms of the density difference due to the added sediment ($\Delta\rho_C$) and density of fresh water (ρ_0). By equating Equations (6) and (7), the settling velocity within the convectively unstable nose region is shown to be related to the reduced gravity of the sediment layer and viscosity as,

$$w_S \equiv (g_C' \, v)^{1/3} \tag{8}$$

Therefore using Equation (6), the time-scale ($T_C = L_C \, / \, w_s$) for a particle of velocity w_S to fall into the unstable nose region of thickness L_C would be given by,

$$T_C = \left(\frac{v}{g'_C{}^2}\right)^{1/3} \tag{9}$$

Note that this expression does not contain the Stokes settling velocity (w_S). This resulting time-scale (T_C), is the fundamental time-scale for the convective sedimentary instability, and has been used in a number of important recent studies to non-dimensionalize the time-scales of various numerical simulations (Burns & Meiburg 2012, 2015; Shao *et al.*, 2017). Their resulting 3D simulations suggest that it takes of order 100 time-scales for fully developed settling-driven convection to develop. This convective time-scale will subsequently be used in this paper to determine the experimental length-scale over which sediment is lost from the bottom of a surface plume. From this point onwards, c_t will be defined as the dimensionless multiple of the time in Equation (9) that takes for settling-driven convection to develop, and the value of c_t will be determined experimentally. It will be assumed that the sedimentary convective time-scale of Burns & Meiburg (2012, 2015) is the relevant time-scale for sediment to be lost from the sharp density interface beneath the overflow so that $T_S = T_C$. With this assumption, Equations (3) and (9) can be combined to estimate a propagation length-scale (L_{prop}) for the gravity current as,

$$L_{prop} \sim \text{Fr}\left(g\frac{\Delta\rho_S}{\rho_0}H\left(1 - \frac{1}{R_\rho}\right)\right)^{1/2} v^{1/3}\left(g\frac{\Delta\rho_C}{\rho_0}\right)^{-2/3} \qquad (10)$$

To see the dependence on R_ρ even more clearly, by keeping the salinity anomaly $\Delta\rho_S$ constant and assuming Fr ~ 1, then two dimensional constants are introduced, $c_1 = (g\,\Delta\rho_S\,H\,/\,\rho_0)^{1/2}$ and $c_2 = v^{1/3}\,(g\,\Delta\rho_S\,/\,\rho_0)^{-2/3}$, with units of m s^{-1} (speed) and s (time) respectively. This reduces the propagation length-scale to a simple function of R_ρ as,

$$L_{prop} = c_1 c_2 c_t \left(1 - \frac{1}{R_\rho}\right)^{1/2} R_\rho^{2/3} \qquad (11)$$

where the combined coefficients $c_1 c_2$ (assuming $\rho \approx \rho_0$) can be furthermore simplified to provide a scale constant (with units of m) as,

$$c_1 c_2 = H^{1/2}\, v^{1/3}\left(g\frac{\Delta\rho_S}{\rho}\right)^{-1/6} \qquad (12)$$

The propagation length-scale (L_{prop}) in Equation (11) goes to zero as R_ρ approaches unity (when there is no density difference between the two layers) and it increases as $R_\rho^{2/3}$ for large R_ρ. For

the case of $R_\rho < 1$ an underflow would occur as the plume would be initially denser than the receiving environment.

RESULTS

Evolution of the current is related to density ratio

The striking differences in the behaviour of the sediment-laden current can be seen in the photograph time series from experiments (Figs. 4, 5 and 6). In particular, the propagation length-scale of the plume is a strong function of the density ratio and decreases as R_ρ gets close to one. Secondary turbidity currents are also seen to form most strongly as R_ρ gets close to unity. In all cases, the changes in behaviour are tied to the vigour of settling-driven convection that strongly increases as R_ρ decreases towards unity.

The speed at which sediment-laden plumes sink beneath the surface plume increases dramatically with decreasing R_ρ (Fig. 4). The series of photographs in Figure 4 depicts the behaviour of the overflow every 30 s for $R_\rho = 3.051$ and 1.48 (left and right panels respectively). The higher value $R_\rho = 3.051$ in Figures 4A to 4J means there is less sediment, and results in weak settling-driven convection. On the other hand for a smaller density ratio of $R_\rho = 1.48$, Figures 4K to 4T depicts a very vigorous mode of settling-driven convection, which resulted in the rapid sinking of distinct finger-like structures. Figures 4J and 4Q display evidence of settling to the bottom after 270 s and 180 s respectively. These corresponds to vertical velocities of approximately $w = 0.14 \times 10^{-3}$ m s^{-1} for $R_\rho = 3.051$, whereas for $R_\rho = 1.48$ the vertical velocity is faster with $w = 2.2 \times 10^{-3}$ m s^{-1}. For comparison, the Stokes settling velocity of an individual particle is 7.7×10^{-5} m s^{-1}, and hence the estimated time from the Stoke settling velocity for a single SiC particle to go from the top to the bottom of the experimental tank is 2 hr. Thus, Figure 4 shows that settling-driven convection at low density ratios has a substantial effect on increasing the downward velocity of collections of SiC particles.

The shapes of the sinking sediment-laden fingers also change with increasing density ratio as displayed in Figure 5. These close-up images illustrate the reduction in width and velocity of the convective sediment fingers as density ratio increases. Figure 5 displays zoomed in photos, taken

every 30 s, and shows weaker settling-driven convection for R_ρ = 4.575 and a much more vigorous settling-driven convection for R_ρ = 1.229. The vertical distance moved by fingers between images indicate faster velocities for R_ρ = 1.229, where the fingers of sediment were wider and formed earlier (compared to R_ρ = 4.575). The vertical velocity of the small plumes (for R_ρ = 4.575) and the large fingers (for R_ρ = 1.229) can be estimated as $w = 6 \times 10^{-4}$ m s^{-1} and $w = 3 \times 10^{-3}$ m s^{-1} respectively (similar to Figure 4). A general trend in both Figures 4 and 5 is that as density ratio decreases towards unity, the surface current moved slower horizontally and the formation of finger-like structures occurred earlier. With the increase in the mass of particles for lower R_ρ, the sediment settled faster as well as entraining water out of the current (as described before by Maxworthy (1999) and Sutherland *et al.* (2018)). Therefore, the head of the current decreased in size and could eventually stop before the end of the tank if settling-driven convection was vigorous enough.

In many experiments, the intense settling-driven convection could form a turbid interflow or an intense turbidity current beneath the buoyant plume (Fig. 6). The series of photos in Figure 6, taken every 60 s, displays these two distinct behaviours of flow for R_ρ = 1.172 and R_ρ = 1.054. In both cases the current moved visibly slower (in the horizontal direction) than those discussed earlier in Figure 5. As can be seen in Figure 6, both currents never reached the end of the tank and stopped before passing 1.5 m, as the sediments settled rapidly due to the very vigorous settling-driven convection of SiC particles. In Figures 6E to 6J, corresponding to R_ρ = 1.172, after the overflow stopped at L_{prop} = 1.3 m, it was interesting to observe the emergence of an interflow below the initial overflow, which lasted for a long time. In this case not only the sediment particles were falling down but they were also dragging water down with them. However, these plumes were not heavy enough to plunge down to the very bottom of the tank. Therefore, the amount of water that the plume carried with itself became significant (similar observations are reported in Sutherland *et al.* 2018). On the other hand, for R_ρ = 1.054 the overflow stopped at a shorter distance of L_{prop} = 0.75 m and an underflow occurred shortly after. This formation of a secondary underflow is consistent with observations first made by Maxworthy (1999).

Horizontal propagation of the current is related to density ratio

The difference between the horizontal velocities of the buoyant plumes with various density ratios can be determined from a series of horizontal photos of the top 0.127 m of the overflow (Fig.7). The standard equation for the velocity in a buoyant plume (Eq. 3) predicted that the horizontal velocity would scale with density ratio as $U \sim (1 - 1 / R_\rho)^{1/2}$, i.e. the velocity decreases as R_ρ approaches one, where there is no density difference. Equation (3) is governed by the dimensionless Froude number, which has usually been found to be between 0.5 to 1 in many previous experiments (i.e. Turner, 1979; Simpson, 1982; Gladstone & Pritchard, 2010; Snow & Sutherland, 2014). As an illustration of this, three cases of R_ρ = ∞, 2.492 and 1.172 are considered here. The speed of the overflow was determined by fitting the best line to the front of the current in each stack of images. The speeds corresponding to the density ratios under consideration were $U_{(R\rho = \infty)}$ = 0.0279 m s^{-1}, $U_{(R\rho = 2.492)}$ = 0.0246 m s^{-1} and $U_{(R\rho = 1.172)}$ = 0.0068 m s^{-1}. Note that for R_ρ = 1.172 the gravity current stopped at L_{prop} =1.3 m, as was also displayed in Figure 6. The comparison of the initial speed of the propagating overflow in the three figures shows a faster speed for the larger density ratios, consistent with the scaling of Equation (3). Using the observed experimental speeds, Equation (3) then determines the Froude number for R_ρ = ∞ to be Fr$_{(R\rho = \infty)}$ = 0.820. Furthermore, estimations of the Froude number based on Equation (3) for R_ρ = 2.492 and 1.172 are Fr$_{(R\rho=2.492)}$ = 0.880 and Fr$_{(R\rho=1.172)}$ = 0.506 respectively. These estimates of the dimensionless Froude numbers are all within the expected range of 0.5 to 1 from previous experiments (i.e. Turner, 1979; Simpson, 1982; Gladstone & Pritchard, 2010). It is also noteworthy in Figure 7 that in all three cases there appears to be no influence from the end wall on these estimates of propagation speed, as the horizontal velocity is constant with time up to the point where plumes hit the wall.

There is very good quantitative agreement between the theoretical prediction of Equation (11) and experimental results of the propagation length-scale of the sediment-laden gravity current as a function of density ratio (Fig. 8). This is the most important result in this paper, and Figure 8 shows that the propagation length-scale decreases to zero as density ratio decreases to one. For R_ρ less than one a plunging flow would occur. The data points are surrounded by two curves in blue, which provides upper and lower bounds on the constants c_1 and c_2 in Equation (12). For experimental conditions in the current study, where 2.9 kg m^{-3} $\leq \Delta\rho_S \leq$ 3.7 kg m^{-3}, the two constants are in the range of 0.0380 $\leq c_1 \leq$ 0.0619 m s^{-1}and 0.0967 $\leq c_2 \leq$ 0.1848 s, so that the

product of $c_{1avg} c_{2avg}$ = 0.0069 m. As outlined earlier, previous numerical simulations of Burns & Meiburg (2012, 2015) suggest that it will take several hundred time-scales for large "finger" instabilities to develop, and so in Figure 8 the blue theoretical curves are plotted to have values of c_t = 440 and 500. These two values bracket the observations well and are consistent with the expectation that c_t is of order 100. For typical values of c_1 and c_2 in ~~lab~~ laboratory conditions, with $1 < R_\rho < 2$, the propagation length-scale is predicted to be $0 < L_{prop} \leq 1.83$ m. Furthermore, for any $R_\rho > 1.3$ in the conducted experiments the observed propagation length-scale (L_{prop}) was limited to the tank length of 1.83 m. It is important to note that all these observations have length-scales dramatically smaller than the prediction of L_{prop} based on the Stokes particle settling rate in Equation (1). The much smaller length-scale is a direct result of the increase rate of particle loss under the influence of settling-driven convection process.

DISCUSSION

Density ratio predicts the sedimentation pattern

The fluid dynamics of the convective sedimentation beneath a buoyant river plume are strongly influenced by the density ratio, as summarized in Figure 9. In the experiments with lower sediment concentrations ($R_\rho > 2$), weak settling-driven convection and slow sinking of particles (e.g. $w = 6 \times 10^{-4}$ m s^{-1}) were observed, in experiments that lasted for a long duration of time (e.g. t = 45 min). On the other hand, when $1.3 < R_\rho < 2$ fingers of sediment were rapidly sinking with much greater vertical velocities of $w = 0.3 \times 10^{-3}$ m s^{-1} under the direct effect of strong and vigorous settling-driven convection. In both of the above-mentioned cases the current reached the end wall, so that L_{prop} = 1.83 m for these experiments in Figure 8. For higher sediment concentrations with $1.17 < R_\rho < 1.23$, the surface plume stopped well before reaching the end wall. In these cases, a slow moving sediment-laden interflow occurred beneath the surface plume. Finally, for cases where R_ρ was very close to unity not only the surface flow stopped, but also an intense underflow was observed. In a much longer tank, it is likely that all the flows would have stopped, and hence formed some sort of subsurface gravity current. However, it is noteworthy that the only intense secondary underflow occurred when $R_\rho \sim 1$. It is very challenging to interpret isolated field observations beneath a river plume. Hence, the images and animations of these various experiments (Supplementary material) when combined with

field estimates of R_ρ could provide a useful guidance for interpretation of data and the possible design of future field observation campaigns.

The most important results of the current set of experiments is that Equation (11) quantifies the length-scale over which it is likely that a surface sediment-laden plume can transform into a subsurface turbidity current (Fig. 10). In lakes with smaller lengths than L_{prop} the sediment is expected to rain down uniformly over the lake bed, possibly with some size fractionation with larger particles closer to river mouth. However, if L_{prop} is sufficiently small compared to the size of the lake, then a secondary turbidity current could form and deposit sediments far from the river mouth, which are often ponded in the deepest regions of the basin. These two forms of sedimentation will result in quite different stratigraphy in lakes' beds, which can then be used to infer paleoclimate records of inflow events (Gilbert & Butler, 2004; Cossu *et al*., 2015).

The mechanism of transforming a buoyant sediment-laden plume into a secondary turbidity current was first expressed by Maxworthy (1999) and greatly popularized in the sedimentology literature by Parsons *et al*. (2001). This process is often invoked as a potential mechanism by which turbidity currents can form, given that typically sediment loads in rivers are not high enough to directly form hyperpycnal underflows (Mulder & Syvitski, 1995; Mulder & Chapron, 2011). Equation (11) can now be used to rigorously quantify when secondary turbidity currents are likely to form. The experimental observations and theoretical predictions in this study confirm that the propagation length-scale of such a flow can dramatically change once density ratio gets very close to unity and it scales as $L_{prop} \sim (1 - 1 / R_\rho)^{1/2} R_\rho^{2/3}$. When R_ρ is less than one, an underflow would form. It is expected that sediment-laden river inflows into lakes will typically have much lower density ratios than in the coastal ocean, so that the behaviour of sedimentation and deposition scales will be very different for the same sediment load in a river (Fig. 9). When a river flows into a lake, the density difference arises due to the temperature anomaly (rather than the salinity difference). The largest density anomaly expected in most lakes might be a 20 °C river flowing into a 10 °C lake, so that $g \, \Delta\rho_S / \rho = 0.0146$ m s^{-2}. In contrast, for a fresh river entering the ocean saline water the reduced gravity would be of order $g \, \Delta\rho_S / \rho = 0.294$ m s^{-2}, i.e. at least 20 times greater. Thus, for the same sediment load, R_ρ is always much larger than one in the ocean and much closer to one in a lake. Underflows are frequently

observed in rivers entering lakes (see for example Fig.19D-2 in Talling *et al.* 2013, and Cossu *et al.* 2015), whereas only very rarely do rivers have enough sediment load in the ocean to form underflows (Mulder & Syvitski, 1995; Mulder & Chapron, 2011). As an example, Hughes Clarke *et al.* (2014) describe typical sediment concentrations as usually being less than 0.07 kg m^{-3} in the Squamish River. In the coastal ocean this is clearly insufficient to form an underflow directly, and the estimated density ratio would be $R_\rho \sim$ 25 kg m^{-3} / 0.07 kg m^{-3} $\sim$ 350. In contrast, if this same river flowed into a thermally stratified lake with a large 10 °C difference across the thermocline, it would have $R_\rho \sim$ 1.5 kg m^{-3} / 0.07 kg m^{-3} $\sim$ 20, and could potentially even have $R_\rho \sim$ 1, if the temperature difference between river and lake was less than 1 °C. For R_ρ $\gg$ 1 then $L_{prop} \sim R_\rho^{2/3}$, so the difference in propagation length between R_ρ = 20 and 350 is a factor of 100, indicating a substantial difference in the likely deposition behaviour between a lake and the ocean.

From laboratory experiments to the field

The idea from Parsons *et al.* (2001) that settling-driven convection can lead to formation of turbidity currents has been often invoked to explain field observations of turbidity currents, but only a few field studies detail some of the causal links. For instance, Hizzett *et al.* (2017) noted that the occurrence of turbidity current below the delta of the Squamish River correlated best with the presence of sediment-laden river plumes, rather than slope failures on the delta. In addition, Schue *et al.* (2015) studied a sediment-laden river plume flowing into a thermally stratified Alpine lake, and observed (using acoustic backscatter) that the vertical velocity of a descending sediment layer below a river plume was an order of magnitude greater than Stokes settling velocities, consistent with the experimental plumes in Figure 4. Furthermore, Giovanoli (1990) studied the transport of sediments from Rhône River flowing into Lake Geneva as an interflow. As mentioned in this study, the sediment concentration in the Rhône River is in the range of 10 − 5000 mg l^{-1}. With the assumption that there is a 10 °C temperature difference between the two layers, it would result in a density ratio within the range of 0.3 < R_ρ < 150 (R_ρ $\sim$ 1.5 kg m^{-3} / 5 kg m^{-3} $\sim$ 0.3 and $R_\rho \sim$ 1.5 kg m^{-3} / 0.01 kg m^{-3} $\sim$ 150). When R_ρ < 1 in Rhône River underflows would form, while for 1 < R_ρ < 150 there is the potential that settling-driven convection could be important underneath the Rhône River.

Application of experimental results to river flows into the coastal ocean

Rivers only occasionally have sufficient suspended sediment to have a density that exceeds that of sea water, when they would immediately form plunging flows (Mulder & Syvitski, 1995). Faster flowing rivers are able to erode and carry more sediment, so it is expected that if underflows could form, it is during flooding events. Empirical data has often be used to find a relationship between the suspended sediment concentration (C_s with units of kg m^{-3}) and the flow rate of the river (Q with units of m^3 s^{-1}) of the form

$$C_S = a\, Q^b \tag{13}$$

where a and b are empirical rating coefficients. Furthermore, Mulder & Syvitski (1995) show that the increased concentration of sediment during a flood ($C_{s\ Flood}$) is related to the average concentration $C_{s\ Average}$ as

$$C_{S\ Flood} = C_{S\ Average} \left(\frac{Q_{Flood}}{Q_{Average}}\right)^b \tag{14}$$

where Q_{Flood} and $Q_{Average}$ are the flow rates during a flood and average conditions. An underflow would occur if $C_s > \Delta\rho_{SeaWater}$. For typical 15 ºC and 35 ppt salinity seawater the density difference with fresh water is $\Delta\rho_{SeaWater} = 25.9$ kg m^{-3} and hence, an underflow happens when $C_s > 25.9$ kg m^{-3}. Mulder & Syvitski (1995) show that a large number of "moderately dirty" rivers could produce underflows (i.e. $R_\rho < 1$) with $b < 1$ (Table 3 in Mulder & Syvitski 1995). For "moderately clean" rivers on the other hand, many would need to have $1 < b \leq 1.5$ (Table 4 in Mulder & Syvitski 1995) to occasionally produce underflows, whereas "relatively clean" rivers would need $1.5 < b \leq 2$ (Table 5 in Mulder & Syvitski 1995) to ever be able to form underflows.

One of the key results of this experiment was to identify that there is a distance over which a surface buoyant plume would lose most of its sediment. Hence, rather than an underflow requiring that a river be denser than seawater, previous papers have suggested that settling-driven convection should allow the sediment in many rivers to be able to convert to a turbid underflow (i.e. Parsons *et al.,* 2001). In order to use the scaling of Equation (14) to estimate the length-scale of propagation of a buoyant plume, the density ratio can be re-written as

$$R_\rho \equiv \frac{\Delta\rho_S}{\Delta\rho_C} \equiv \frac{\Delta\rho_{SeaWater}}{C_{S\,Flood}} \times (\frac{Q_{Average}}{Q_{Flood}})^b \qquad (15)$$

Therefore, while the condition of Mulder & Syvitski (1995) requires $R_\rho \leq 1$ for underflow formation, the experiments conducted in this study show that in many cases a secondary turbidity current can form in a distance that increases with R_ρ.

It is helpful to consider when there might be sufficient sediment load in the Squamish River in BC, Canada to form underflows (Fig. 11). This particular river is a good example of a sediment-laden river that is known to form periodic underflows (Hizzett $et\,al.$ 2017). Data from Table 3 in Mulder & Syvitski (1995) suggests that $C_{s\,Average} = 1$ kg m^{-3}, $Q_{Average} = 58$ m^3 s^{-1} and $b \leq 1$ for this river. In this case, assuming $b = 1$, then when $Q_{Flood} = 1502$ m^3 s^{-1}, the ratio $Q_{Flood} / Q_{Average} = 25.9$ would predict $R_\rho = 1$. Any higher flow rate would have $R_\rho < 1$ and so for all higher values of Q a plunging flow would form. For normal flow conditions however, the density of suspended sediment is $C_{s\,Average} = 1$ kg m^{-3}, which would predict $R_\rho = 25.9$. Hence, it is instructive to plot the predicted length-scale (L_{prop}) as a function of flow rate values (Q) in Figure 11. In this figure, depth of the river is assumed to be $H = 10$ m (note that the constant in Equation (11) depends on $H^{1/2}$ and hence the result is not very sensitive to exact choice of this values, which would also fluctuate with tides). In Using Equation (11), the predicted length-scale of deposition for the Squamish River is 136 m for the average flow rate value of $Q_{Average} = 58$ m^3 s^{-1}, and up to 1 - 2 km for lower flow rate values (Fig. 11). While there are no direct observations of settling-driven convection below the Squamish River, the predicted length-scales of 100s to 1000s of meters are broadly consistent with the distributions of sediment from the Squamish River within Howe Sound (i.e. Figure 2 in Gales $et\,al.$ 2018). The exact relationship between R_ρ and Q for a specific river would require more research – for instance the average value of observed suspended sediment concentrations made by Hughes Clarke $et\,al.$ (2014) was 0.07 kg m^{-3} in the Squamish River, notably less than the value of $C_{s\,Average} = 1$ kg m^{-3} described by Mulder & Syvitski (1995).

Important differences between laboratory experiments and the field

The real world is much more complicated than the idealized experiments performed in this paper. The major benefit of laboratory experiments is that they can be used to study one specific

process in isolation so that the controlling parameters can be quantified. On the other hand, the disadvantage is that when applying such scaling of the length-scale to a field setting, there may be many other processes that could also be important. Hence, it is critical to discuss the significant differences that might influence the interpretation of results in this paper. One important difference is that the current set of experiments had a finite volume of sediment-laden fluid that entered the ambient - these are the so-called "dam break" experiments and are widely used in fluid dynamics laboratory experiments (i.e. Turner, 1979; Simpson, 1982; Gladstone & Pritchard, 2010). A real river however has a constant inflow, with new material continuously being pushed out from the river mouth. Therefore, even if most of the sediment is settling out from the river plume in a distance L_{prop}, the surface layer would still be pushed out by the continuous supply of water. Hence, the surface plume could continue to move out into the water body many kilometers, even after settling has occurred. Thus, the length-scales shown in Figure 11B are probably lower bounds on what the length-scale of the surface plume would look like in the field. In addition, Equation (11) implicitly assumes that the plume only spreads in one dimension, as in the laboratory. This is probably a reasonable assumption for the Squamish River spreading in the long fjord of Howe Sound, but in many coastal settings, river plumes are unconstrained and will spread in two-dimensions (Horner-Devine *et al.*, 2015). Secondary turbidity currents are also more likely to occur when there is a sloping bottom, as opposed to the uniform depth in these experiments. For instance the experimental setup in the studies made by Parsons *et al*. (2001), Snow & Sutherland (2014) and Sutherland *et al*. (2018) all included a sloping ramp, which would probably increase the tendency to form turbidity currents beneath an overflow.

Another critical process that occurs when fine river sediments meet the ocean is flocculation, which can also dramatically increase settling rates as flocs of particles sink faster than an individual particle. Flocculation is typically promoted at the pycnocline due to ionic exchange and other processes, so where fresh water enters a saline body, flocculation may be more likely. The increases in settling of sediment particles by flocculation could be occurring at the same time as settling-driven convection, so future work would need to determine the relative importance of such processes in estuaries. In real rivers there will also be a distribution of sediment particle size, rather than the uniform particles used in this study. Larger particles can

sink into the "nose region" of Figure 2B faster than small particles, so there is weak dependence on the instability time-scale of Equation (9), as observed in the 3D simulations of Burns & Meiburg (2015) and experimental observations of Sutherland *et al.* (2018). While some numerical work (i.e., Burns & Meiburg, 2012, 2015; Yu *et al.*, 2014, 2015) and experimental studies (Sutherland *et al.*, 2018) have suggested a weak dependence of the vigour of settling-driven convection on particle size, this remains an important area of future work. The main effect of a particle distribution will be some degree of fractionation of particles, with the larger particles being deposited closer to river mouth, and smaller particles settling at great differences from river mouth.

Tidal currents have also been shown to be somewhat important in triggering of turbidity currents in locations in British Columbia such as the Squamish River (Clare *et al.,* 2016) and the Fraser delta (Ayranci *et al.,* 2012; Lintern *et al.,* 2016). While Clare *et al.* (2016) found that surface sediment-laden plumes at Squamish were linked to ~70% of all turbidity currents; the precise timing was also strongly affected by tidal elevation. At low tides at Squamish, more (and coarser) sediment was flushed off the delta top, which increased the sediment flux and had higher settling rate due to coarser grains being transported. This tidal influence overprints the original signature of river discharge (Clare *et al.,* 2016). At low tides, it is also possible that the shallow water depth may also promote formation of turbidity currents as there would be less dilution of the sediment-laden convective fingers, similar to how the sloping ramp promoted the formation of turbidity currents in experiments of Parsons *et al.* (2001), Snow & Sutherland (2014) and Sutherland *et al.* (2018).

Possible applications of experiments to other systems

A recent paper by Stack *et al.* (2018) has tried to extrapolate some of the dynamics of sediment-laden rivers on Earth to understand ancient geological formations on Mars that possibly formed underwater. Specifically when trying to explain the geology of the Murray formation they speculate about the conditions under which an ancient Martian river could form an underflow in the Gale crater. A starting point for their discussion is that the evidence for geological deposits associated with a plunging river plume implies that the density of the river water be greater than that of the receiving waters (i.e. that $R_\rho \leq 1$). From various estimates of

the possible sediment load in river they draw inferences as to how salty the water body could have been. The analysis in this paper hopefully shows that in many situations plunging underflows can also form for $R_\rho > 1$ due to the active settling-driven convection at the base of the overflow. Hence, the estimates by Stack *et al.* (2018) of the salinity of ancient water bodies in the Gale crater are possibly lower bounds, which have important implications for life on Mars.

A final area where the dynamics of settling-driven convection is relevant is in the dynamics of pyroclastic flows, especially in how a hot volcanic ash cloud might intrude into the thermally stratified atmosphere. Indeed the current work is related to previous experiments of Carazzo & Jellinek (2012, 2013), Manzella *et al.* (2015) and Scollo *et al.* (2017), who studied the dynamics of settling-driven convection in order to interpret field observations of ash-laden volcanic clouds. In particular, geologists often wish to know the radius over which ash will deposit, as this has important hazard prediction implications. Equation (11) could be used to help estimate this radius – the major difference being that the air has a much lower viscosity than water, which will tend to enhance the rate at which the instability forms. The video imagery provided in the Supplementary material might further help interpret the finger like sediment plumes often seen in field observations of volcanic ash clouds (Scollo *et al.*, 2017).

CONCLUSION

The main finding of this paper is that settling-driven convection can result in the rapid loss of sediment below a buoyant plume. The length-scale of sediment deposition is determined by the length-scale over which the plume propagates, and the faster sediment loss due to settling-driven convection results in a far smaller propagation length-scale compared to a simple estimate made by the Stokes settling velocity. The vertical settling of dense sediment-laden plumes was measured to be as much as 100 times that of the Stokes settling velocity of an individual particle. For density ratios close to unity, the propagation length-scale was small and an intense underflow or interflow emerged, which propagated longer distance than the surface plume. However, when density ratio was larger than one this length-scale increased as $R_\rho^{2/3}$. For a given salt stratification in an estuary, or thermal stratification in a lake, the sediment difference between the surface and deep layers will determine the strength of settling-driven convection.

The sediment load in a river can be estimated by using a rating curve for the sediment load as a function of river flow rate (Q). Hence, it is possible to estimate the density ratio (R_ρ) as a function of Q for a river flowing into a salty ocean. Equation (11) can then be used to predict the length-scale over which sedimentation could occur, as was done in the example of the Squamish River. In these oceanic cases it is reasonable to ignore temperature effects, as large salinity differences dominate the density differences. To make the same estimates using Equation (11) for a lake, it would also require that the temperature of the river and the seasonal thermal stratification of the lake be known. For example, Cossu *et al*. (2015) discussed how the seasonality in sediment loading in rivers and changes of the thermal stratification in an alpine lake could greatly influence whether overflows, interflows or underflows occurred. Hopefully, future research into these processes will include measurements of the density ratio, and the design of field observations can be guided by the predictions of Equation (11) and the time-lapse movies contained in the Supplemental section.

NOMENCLATURE

a	Empirical rating coefficient
b	Empirical rating coefficient
C	Average concentration of the flow (kg m^{-3})
C_s	Concentration of suspended sediment (kg m^{-3})
$C_{s\,Average}$	Average concentration of suspended sediment (kg m^{-3})
$C_{s\,Flood}$	Concentration of suspended sediment during a flood (kg m^{-3})
c_t	Dimensionless multiple of time that takes for settling-driven convection to develop
C_0	Initial concentration of the flow (kg m^{-3})
c_1	1st dimensional constant (m s^{-1})
c_{1avg}	Average value of the 1st dimensional constants (m s^{-1})
c_2	2nd dimensional constant (s)
c_{2avg}	Average value of the 2nd dimensional constants (s)
Fr	Froude number
g	Gravitational acceleration (9.81 m s^{-2})
g'	Reduced gravity (m s^{-2})
g'_C	Reduced gravity in terms of density difference due to the added sediment (m s^{-2})
Gr	Grashof number
H	Thickness of the current (m)
$\overline{H}$	Mean thickness of the current (m)
L_C	Thickness of the nose region (m)
L_{prop}	Propagation length-scale of the current (m)
m_C	Mass of sediment particles (kg)
m_{comp}	Mass of the water in the small compartment (kg)
Q	The flow rate of a river (m^3 s^{-1})
$Q_{Average}$	Average flow rate of a river (m^3 s^{-1})
Q_{Flood}	Flow rate of a river during flood (m^3 s^{-1})
Re	Reynolds number
R_ρ	Density ratio

NOMENCLATURE CONTINUED

T_S	Settling time-scale of sediment particles (s)
t	Time (s)
t_{comp}	Temperature of the small compartment (°C)
t_S	Temperature of the saline ambient (°C)
t_0	Time corresponding to the initial stable density profile (s)
U	Horizontal velocity of the current (m s^{-1})
V_{comp}	Volume of the compartment (m^3)
w	Vertical velocity of the fluid in the nose region (m s^{-1})
w_S	Stokes settling velocity of sediment particles (m s^{-1})
$\Delta\rho$	Density difference between the current and the saline ambient (kg m^{-3})
$\Delta\rho_C$	Density differences due to the added sediment (kg m^{-3})
$\Delta\rho_S$	Density differences due to the added salt (kg m^{-3})
$\Delta\rho_{SeaWater}$	Density difference due to the added salt for sea water at 15 °C
Δt	Elapsed time between the stable and the unstable density profiles (s)
φ	Mass concentration of sediment particles (kg kg^{-1})
γ	Density expansion coefficient for SiC particles
v	Coefficient of kinematic viscosity of fresh water at 20 °C (10^{-6} m^2 s^{-1})
ρ	Average density between the current and the saline ambient (kg m^{-3})
ρ_C	Density of the sediment-laden water (kg m^{-3})
ρ_{comp}	Density of the small compartment before adding sediment (kg m^{-3})
ρ_f	Total density of a fluid (kg m^{-3})
ρ_S	Density of the saline ambient (kg m^{-3})
ρ_{SiC}	Density of SiC particles (3210 kg m^{-3})
ρ_0	Density of clear fresh water at 20°C (998.2 kg m^{-3})

REFERENCES

Ayranci, K., Lintern, D.G., Hill, P.R. and **Dashtgard, S.E.** (2012) Tide-supported gravity flows on the upper delta front, Fraser River delta, Canada. *Mar. Geol.*, **326**, 166 – 170.

Benjamin, T.B. (1968) Gravity currents and related phenomena. *J. Fluid Mech.*, **31**, 209 – 248.

Burns, P. and **Meiburg, E.** (2012) Sediment-laden fresh water above salt water: Linear stability analysis. *J. Fluid Mech.*, **691**, 279 – 314.

Burns, P. and **Meiburg, E.** (2015) Sediment-laden fresh water above salt water: Nonlinear stability analysis. *J. Fluid Mech.*, **762**, 156 – 195.

Carazzo, G. and **Jellinek, A.M.** (2012) A new view of the dynamics, stability and longevity of volcanic clouds. *Earth Planet. Sci. Lett.*, **325 – 326**, 39 – 51.

Carazzo, G. and **Jellinek, A.M.** (2013) Particle sedimentation and diffusive convection in volcanic ash-clouds. *J. Geophys. Res. Solid Earth*, **18**, 1420 – 1437, doi:10.1002/jgrb.50155.

Chen, C.F. (1997) Particle flux through sediment fingers. *Deep Sea Res.*, **44** (9 – 10), 1645 – 1654.

Clare, M.A., Clarke, J.H., Talling, P.J., Cartigny, M.J.B. and **Pratomo, D.G.** (2016) Preconditioning and triggering of offshore slope failures and turbidity currents revealed by most detailed monitoring yet at a fjord-head delta. *Earth Planet. Sci. Lett.*, **450**, 208 – 220.

Cossu, R., Forrest A.L., Roop, H.A., Dunbar, G.B., Vandergoes, M.J., Levy, R.H., Stumoner, P. and **Schladow, S. G.** (2015) Seasonal variability in turbidity currents in Lake Ohau, New Zealand, and their influence on sedimentation. *Mar. Freshwater Res.*, doi:10.1071/MF15043.

Davarpanah Jazi, S. and **Wells, M.G.** (2016) Enhanced sedimentation beneath particle-laden flows in lakes and the ocean due to double-diffusive convection. *Geophys. Res. Lett.*, **43** (20), 10883 – 10890, doi: 10.1002/2016GL069547.

Forel, F.A. (1885) Les ravins sous-lacustres des fleuves glaciaires. Comptes Rendus de l'Académie des Sciences de Paris: 1-3.

Geyer, W.R., Hill, P.S. and **Kineke, G.C.** (2004) The transport, transformation and dispersal of sediment by buoyant coastal flows. *Cont. Shelf Res.*, **1212** (24), 927 – 949.

Gilbert, R. and **Butler, R.D.** (2004) The physical limnology and sedimentology of Meziadin Lake, northern British Columbia, Canada. *Arct. Antarct. Alp. Res.*, **36** (1), 33 – 41.

Giovanoli, F. (1990) Horizontal transport and sedimentation by interflows and turbidity currents in Lake Geneva. In *Large Lakes*, edited by Tilzer, M. M. and Serruya, C., pp. 175 − 195, Springer, Berlin.

Gladstone, C. and **Pritchard, D.** (2010) Patterns of deposition from experimental turbidity currents with reversing buoyancy. *Sedimentology*, **57**, 53 − 84.

Green, T. (1987) The importance of double diffusion to the settling of suspended material. *Sedimentology*, **34**, 319 − 331.

Hill, P.S., Milligan, T.G. and **Geyer, W.R.** (2000) Controls on effective settling velocity of suspended sediment in the Eel River flood plume, *Cont. Shelf Res.*, **20** (16), 2095 − 2111.

Hill, P.R., Conway, K., Lintern, D.G., Meulé, S., Picard, K. and **Barrie, J.V.** (2008) Sedimentary processes and sediment dispersal in the southern Strait of Georgia, BC, Canada. *Mar. Environ. Res.*, **66**, S39 − S48.

Hizzett, J.L., Hughes Clarke, J.E., Sumner, E.J., Cartigny, M.J.B., Talling, P. J. and **Clare, M.A.** (2017) Which triggers produce the most erosive, frequent and longest runout turbidity currents on deltas? *Geophys. Res. Lett.*, **45**, doi: 10.1002/2017GL075751.

Horner-Devine, A.R., Hetland, R.D. and **MacDonald, D.G.** (2015) Mixing and transport in coastal river plumes. *Annu. Rev. Fluid Mech.*, **47**, 569 – 594.

Houk, D. and **Green, T.** (1973) Descent rates of suspension fingers. *Deep Sea Res.*, **20**, 757 − 761.

Hoyal, D.C.J.D., Bursik, M.I. and **Atkinson, J.F.** (1999a) The influence of diffusive convection on sedimentation from buoyant plumes. *Mar. Geol.*, **159**, 205 − 220.

Hoyal, D.C.J.D., Bursik, M.I. and **Atkinson, J.F.** (1999b) Settling-driven convection: A mechanism of sedimentation from stratified fluids. *J. Geophys. Res.*, **104** (C4), 7953 − 7966, doi: 10.1029/1998JC900065.

Huppert, H.E. (2006) Gravity currents: a personal perspective. *J. Fluid Mech.*, **554**, 299 − 322.

Hughes Clarke, J.E., Marques, C.R.V. and **Pratomo, D.** (2014) Imaging active mass-wasting and sediment flows on a fjord delta, Squamish, British Columbia. In *Submarine Mass Movements and Their Consequences*, 249 − 260, Springer.

Kineke, G. C., Woolfe, K. J., Kuehl, S. A., Milliman, J. D., Dellapenna, T. M. and **Purdon, R. G.** (2000) Sediment export from the Sepik River, Papua New Guinea: evidence for a divergent sediment plume. *Cont. Shelf Res.*, **20** (16), 2239 − 2266.

Lintern, D. G., Hill, P. R. and **Stacey, C.** (2016) Powerful unconfined turbidity current captured by cabled observatory on the Fraser River delta slope, British Columbia, Canada. *Sedimentology*,

63 (5), 1041 – 1064.

Manzella, I., Bonadonna, C., Phillips, J.C. and **Monnard, H.** (2015) The role of gravitational instabilities in deposition of volcanic ash. *Geology*, **43** (3), 211 – 214.

Martin, D. and **Nokes, R.** (1998) Crystal settling in a vigorously convecting magma chamber. *Nature*, **332**,534 – 536.

Maxworthy, T. (1999) The dynamics of sedimenting surface gravity currents. *J. Fluid Mech.*, **392**, 27 – 44.

Meiburg, E. and **Kneller, B.C.** (2010) Turbidity currents and their deposits. *Annu. Rev. Fluid Mech.*, **42**, 135 – 156.

Mulder, T. and **Chapron, E.** (2011) Flood deposits in continental and marine environments: character and significance. In *Sediment Transport from Shelf to Deep Water — Revisiting the Delivery System*, AAPG Stud. Geol., vol. **61**, edited by R. M. Slatt and C. Zavala, pp. 1 – 30.

Mulder, T. and **Syvitski, J.P.M.** (1995) Turbidity currents generated at river mouths during exceptional discharges to the world oceans. *J. Geol.*, **103** (3), 285 – 299.

Nowacki, D.J., Horner-Devine, A.R., Nash, J.D. and **Jay, D.A.** (2012) Rapid sediment removal from the Columbia River plume nearfield. *Cont. Shelf Res.* **35**, 16 – 28.

Parsons, J.D. and **Garcia, M.H.** (2000) Enhanced sediment scavenging due to double-diffusive convection. *J. Sediment. Res.*, **70** (1), 47 – 52.

Parsons, J.D., Bush, J.W.M. and **Syvitski, J.P.M.** (2001) Hyperpycnal plume formation from riverine outflows with small sediment concentrations. *Sedimentology*, **48** (2), 465 – 478.

Penney, J. and **Stastna, M.** (2016) Direct numerical simulation of double-diffusive gravity currents. Physics of Fluids **28**, 086602; doi: 10.1063/1.4961045.

Rouhnia, M. and **Strom, K.** (2015) Sedimentation from flocculated suspensions in the presence of settling-driven gravitational interface instabilities. *J. Geophys. Res. Oceans*, **120**, 6384 – 6404, doi: 10.1002/2015JC010750.

Rouhnia, M. and **Strom, K.** (2017) Sedimentation from buoyant muddy plumes in the presence of interface mixing: an experimental study. *J. Geophys. Res. Oceans*, **120**, 2652 – 2670, doi: 10.1002/2016JC012053.

Shao, Y.C., Hung, C.Y. and **Chou, Y.J.** (2017) Numerical study of convective sedimentation through a sharp density interface. *J. Fluid Mech.,* **824**, 513 - 549.

Scheu, K.R., Fong, D.A., Monismith, S.G. and **Fringer, O.B.** (2015) Sediment transport dynamics near a river inflow in a large alpine lake. *Limnol. Oceanogr.*, **60** (4), 1195 – 1211.

Simpson, J.E. (1982) Gravity currents in the laboratory, atmosphere and ocean. *Ann. Rev. Fluid Mech.*, **14** (1), 213 – 234.

Snow, K. and **Sutherland, B.R.** (2014) Particle-laden flow down a slope in uniform stratification. *J. Fluid Mech.*, **755**, 251 – 273.

Scollo, S., Bonadonna, C., and **Manzella, I.** (2017) Settling-driven gravitational instabilities associated with volcanic clouds: new insights from experimental investigations. *Bulletin of Volcanology*, **79**:39. https://doi.org/10.1007/s00445-017-1124-x.

Sparks, R.S.J., Carey, S.N. and **Sigurdsson, H.** (1991). Sedimentation from gravity currents generated by turbulent plumes. *Sedimentology*, **38** (5), 839 - 856.

Stack, K. M., Grotzinger, J. P., Lamb, M. P., Gupta, S., Rubin, D. M., Kah, L. C., Edgar, L. A., Fey, D. M., Hurowitz, J. A., McBride, M., Rivera-Hernández, F., Sumner, D. Y., Van Beek, J. K., Williams, R. M. E., and **Yingst, R. A.** (2018) Evidence for plunging river plume deposits in the Pahrump Hills member of the Murray formation, Gale crater, Mars. *Sedimentology,* doi: 10.1111/sed.12558

Sutherland, B.R., Gingras, M.K., Knudson, C., Steverango, L. and **Surma, C.** (2018) Particle-bearing currents in uniform density and two-layer fluids. *Phy. Rev. Fluids*, 3 (2), p.023801.

Talling, P. J., Paull, C.K. and **Piper, D.J.W.** (2013) How are subaqueous sediment density flows triggered, what is their internal structure and how does it evolve? Direct observations from monitoring of active flows. *Earth-Sci. Rev.*, **112**, 244 - 288.

Turner, J. S. (1979) Buoyancy Effects in Fluids. Cambridge University Press.

Warrick, J. A., Xu, J., Marlene, A. N. and **Homa, J. L.** (2008) Rapid formation of hyperpycnal sediment gravity currents offshore of a semi-arid California river. *Cont. Shelf Res.*, **28**, 991 – 1009.

Yuan, Y. and **Horner-Devine, A.R.** (2017) Experimental investigation of large-scale vortices in a freely spreading gravity current. *Phys. Fluids*, 29(10), p.106603. https://doi.org/10.1063/1.5006176.

Yu, X., Hsu, T. J. and **Balachandar, S.** (2013) Convective instability in sedimentation: Linear stability analysis. *J. Geophys. Res. Oceans*, **118**, 256 – 272, doi:10.1029/2012JC008255.

Yu, X., Hsu, T. J. and **Balachandar, S.** (2014) Convective instability in sedimentation: 3-D numerical study. *J. Geophys. Res. Oceans*, **119**, 8141 – 8161, doi:10.1002/2014JC010123.

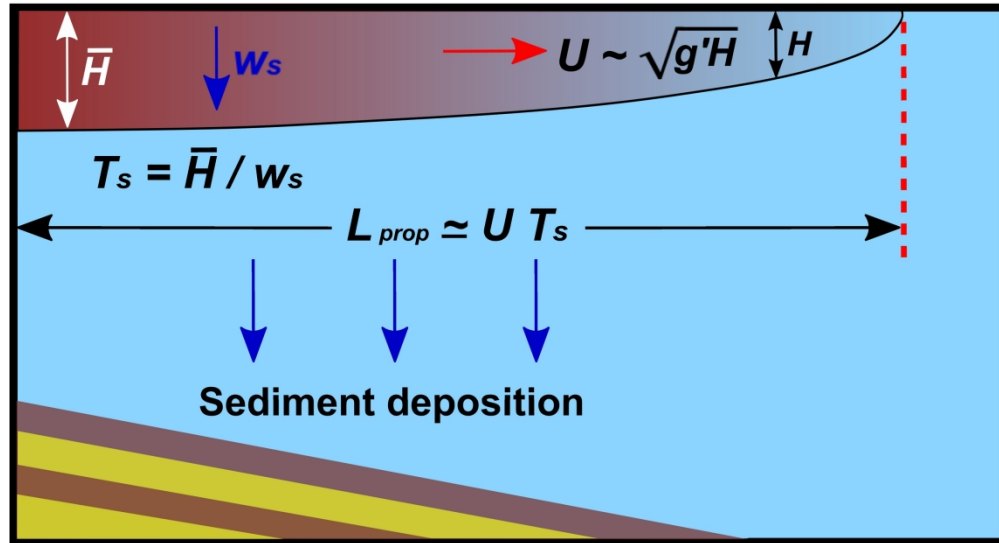**Zhixin, Q., Eames, I.** and **Greig, A.** (2014) Flushing ballast tanks. *Ocean Eng.*, **89**, 157 – 172.

Fig. 1: A conceptual diagram of the relevant scales beneath a buoyant sediment-laden current that propagates on top of a saline ambient as an overflow from a river mouth. The length-scale of sediment deposition is determined by how far the buoyant sediment-laden plume will propagate before the sediment is lost. This current has a mean thickness of H_{bar}, horizontal velocity of U and propagation length of L_{prop}. The Stokes settling velocity of sediment particles within the current is w_S and the settling time-scale of each sediment particle can be represented as T_S.

251x137mm (300 x 300 DPI)
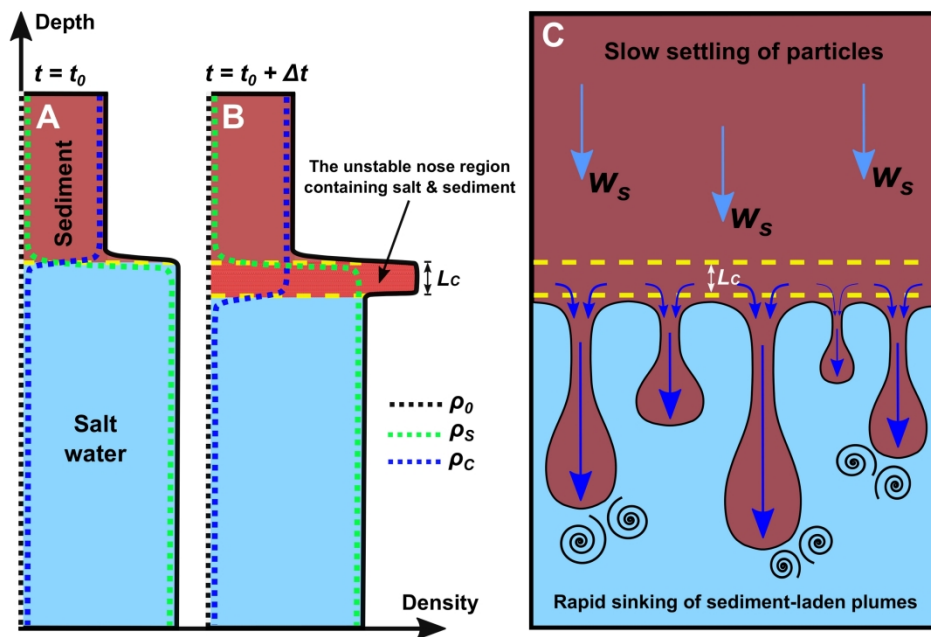
Fig. 2: A schematic representation of the instabilities that lead to settling-driven convection. (A) At time $t = t_0$ the initial density profile is stable, with a lighter sediment-laden overflow above a dense saline layer. Here the added density due to the mass fraction of sediment ($\Delta\rho_C$) is smaller everywhere than the added density due to the added salt ($\Delta\rho_S$) resulting in a stable stratified salt/sediment configuration. (B) At a later time of $t = t_0 + \Delta t$, sediment has settled down producing an unstable nose region containing both salt and sediment. The density of fresh water, salt water and sediment water are specified by ρ_0, ρ_S and ρ_C respectively. The dotted green and blue lines indicate density of salt water (ρ_S), sediment water (ρ_C), while the solid black line represents the total density (ρ_f). The thickness of the unstable nose region is shown as L_C, which has grown with time defined as $L_C = w_S \Delta t$ (Burns & Meiburg, 2012). (C) The nose region can now become unstable, resulting in a process of vigorous settling-driven convection of sediment particles beneath the interface. The descending large finger-like plumes of sediment-laden material have vertical velocities of at least an order of magnitude faster than the Stokes settling velocity of a single particle (w_S).
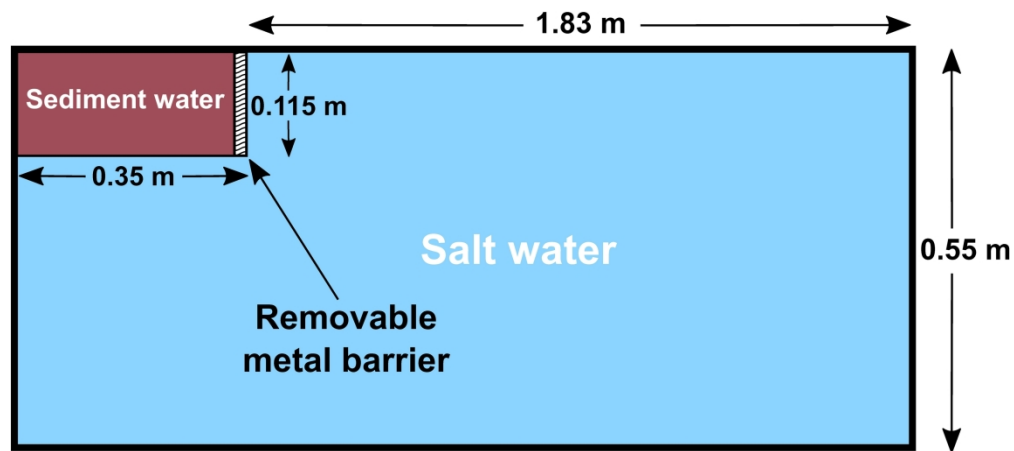
297x210mm (300 x 300 DPI)

Fig. 3: Schematic side view of the experimental setup, showing the main tank (containing saline water), the small isolated compartment on the left-hand side (containing sediment water) and the removable metal barrier. When the barrier is removed, a layer of sediment-laden water propagates on top of the saline ambient, thus simulating the entrance of a buoyant river into a denser lake or the coastal ocean.

288x128mm (300 x 300 DPI)

Table 1: The data corresponding to the conducted experiments

Exp. No.	R_ρ	t_s (ºC)	t_{comp} (ºC)	m_C (kg)	L_{prop} (m)	Flow behavior
1	0.687	16.8	16.2	0.065	-	Strong underflow / Movie S1
2	1.021	18.2	18.2	0.045	0.65	Fig. 9D
3	1.054	18.7	18.8	0.041	0.75	Fig. 9D / Movie S2
4	1.093	19.9	20.1	0.042	1	Fig. 9D
5	1.107	20.7	20.4	0.039	1.1	Fig. 9D
6	1.151	21	20.8	0.034	1.25	Fig. 9D
7	1.172	20.6	20.5	0.038	1.3	Fig. 9C
8	1.230	20.8	20.4	0.034	1.55	Very weak version of Fig. 9D
9	1.233	20.5	20.3	0.035	1.6	Fig. 9C
10	1.308	21	20.6	0.033	1.83	Fig. 9B
11	1.391	20.6	20.6	0.032	1.83	Fig. 9B / Movie S3
12	1.433	18.7	18.8	0.032	1.83	Fig. 9B / Movie S4
13	1.483	20.6	20.5	0.030	1.83	Fig. 9B
14	1.779	20.6	20.6	0.025	1.83	Fig. 9B
15	2.155	20.1	19.9	0.020	1.83	Weak version of Fig. 9B
16	2.492	17.4	19.3	0.020	1.83	Fig. 9A
17	3.051	19.8	19.7	0.015	1.83	Fig. 9A
18	4.575	18.5	18.7	0.010	1.83	Fig. 9A / Movie S5
19	∞	19.7	20.2	0	1.83	Strong overflow / Movie S6

Fig. 4: There is a striking difference in behavior between weak settling-driven convection (R_ρ = 3.051, panels (A) to (J)) and vigorous settling-driven convection (R_ρ = 1.483, panels (K) to (T)). The photos were taken every 30 s and show the differences in vertical velocities of settling-driven convection for the slower case of R_ρ = 3.051 and the faster case of R_ρ = 1.483. Movies S5 (R_ρ = 4.575) and S4 (R_ρ = 1.433) in the Supplemental section respectively show the weak and vigorous settling-driven convection.

175x251mm (300 x 300 DPI)
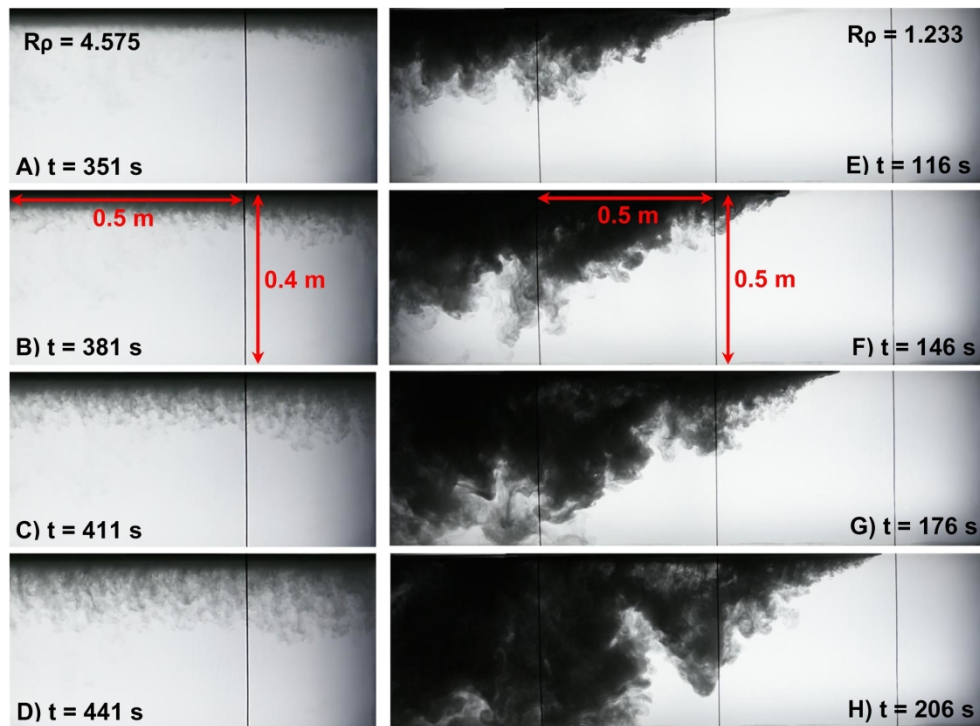
Fig. 5: A series of close up photos that emphasize the form of the settling-driven convection. These images were taken every 30 s. Panels (A) to (D) show slow sinking sediment plumes due to weak settling-driven convection in an experiment with high density ratio (R_ρ = 4.575), while panels (E) to (H) depict faster sinking sediment fingers due to vigorous settling-driven convection in an experiment with low density ratio (R_ρ = 1.229).

177x128mm (300 x 300 DPI)
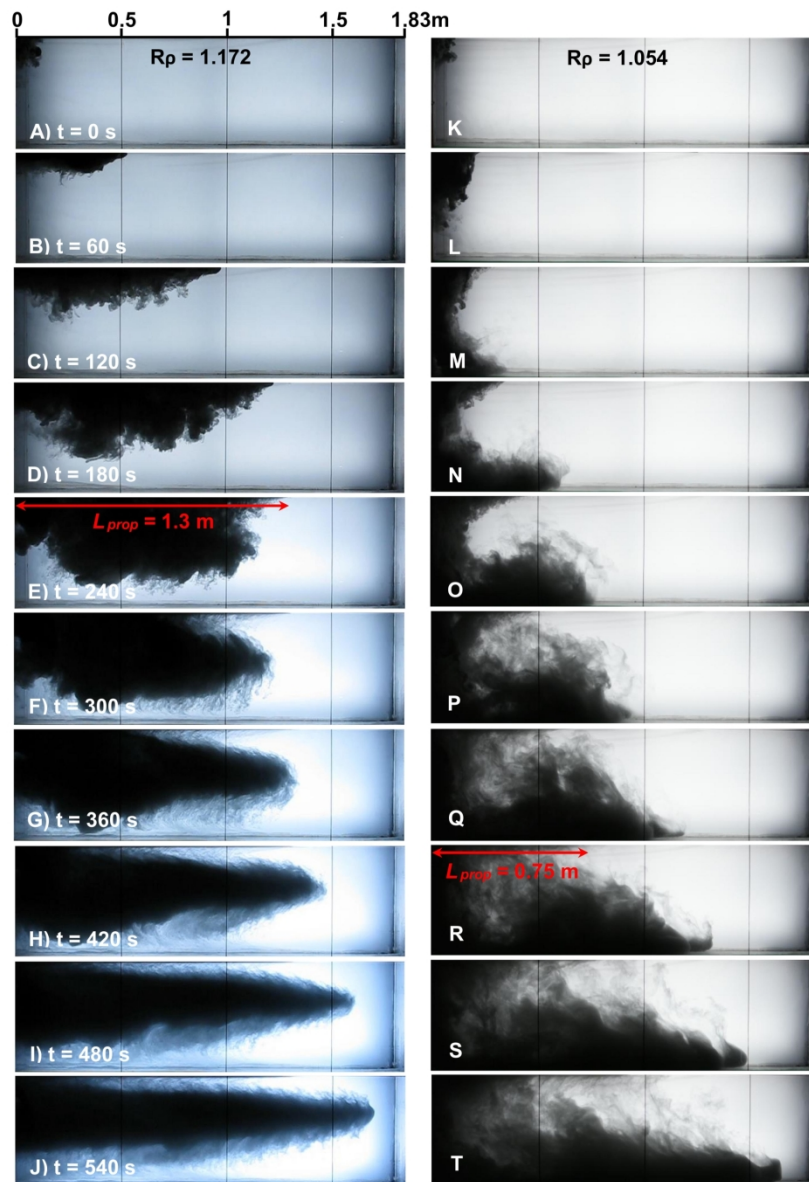
Fig. 6: Photos of experiments taken every 60 s, which shows the formation of (A) to (J) an interflow (R_ρ = 1.172) and (K) to (T) an underflow (R_ρ = 1.054) from the descending mixture of sediment and freshwater into the saline body. In both cases the surface current never reached the end of the tank and stopped before reaching a distance of 1.5 m, as the sediments settled rapidly due to the strongly vigorous settling-driven convection of SiC particles. In Figure 6E the overflow stopped at 1.3 m, whereas in Figure 6R it stopped at 0.75 m. Movies S2 (R_ρ = 1.054) and S3 (R_ρ = 1.391) in the Supplemental section respectively show the emergence of a secondary underflow and interflow.

175x245mm (300 x 300 DPI)
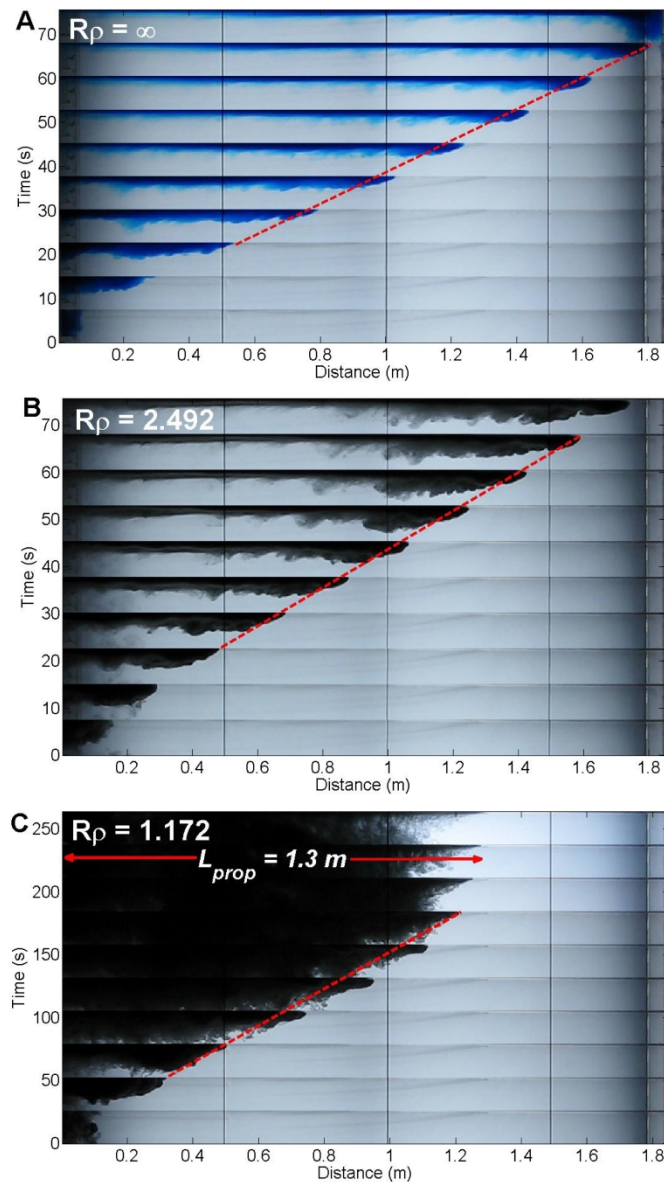
Fig. 7: A time-series of photos taken from the top 0.127 m of the overflow to compare the propagation speed of the gravity current for different density ratios in (A) $R_\rho = \infty$ (speed = 0.0279 m s^{-1}), (B) R_ρ = 2.492 (speed = 0.0246 m s^{-1}) and (C) R_ρ = 1.172 (speed = 0.0068 m s^{-1}), where the gravity current stops at L_{prop} = 1.3 m. The speed of the overflow was determined by fitting the best line to the front of the current in each stack of images. A comparison of the initial speed of the propagating overflow in the three figures shows a faster speed for the larger density ratios that have larger density contrast, which is consistent with the scaling of Equation (3).
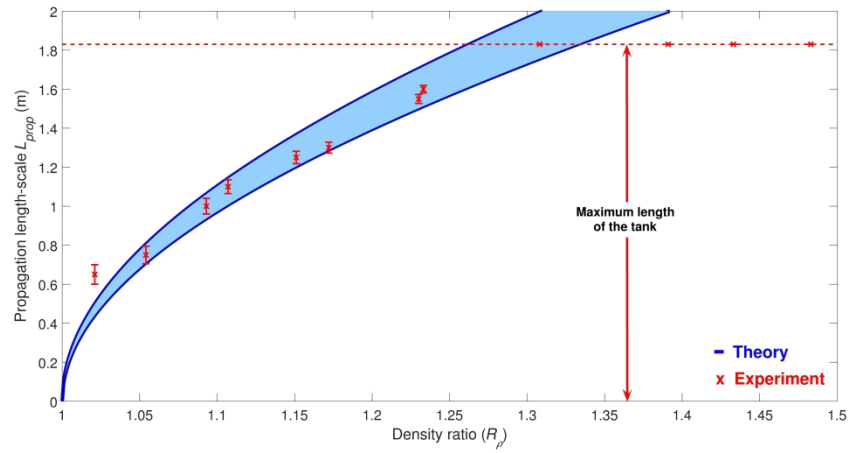
314x551mm (300 x 300 DPI)

Fig. 8: A comparison of theoretical predictions and experimental observations of the propagation length-scale (L_{prop}) of the gravity current as a function of various density ratios (R_ρ). Decreasing R_ρ towards unity results in a decrease in L_{prop}. The two curves for the theory represent a realistic range of values between c_{1avg} = 0.0462 m s^{-1}, c_{2avg} = 0.1489 s, and c_t = 440 and 500 for the coefficient in Equation (11). The length of the tank is 1.83 m, limiting the maximum propagation length-scale of the experiments.
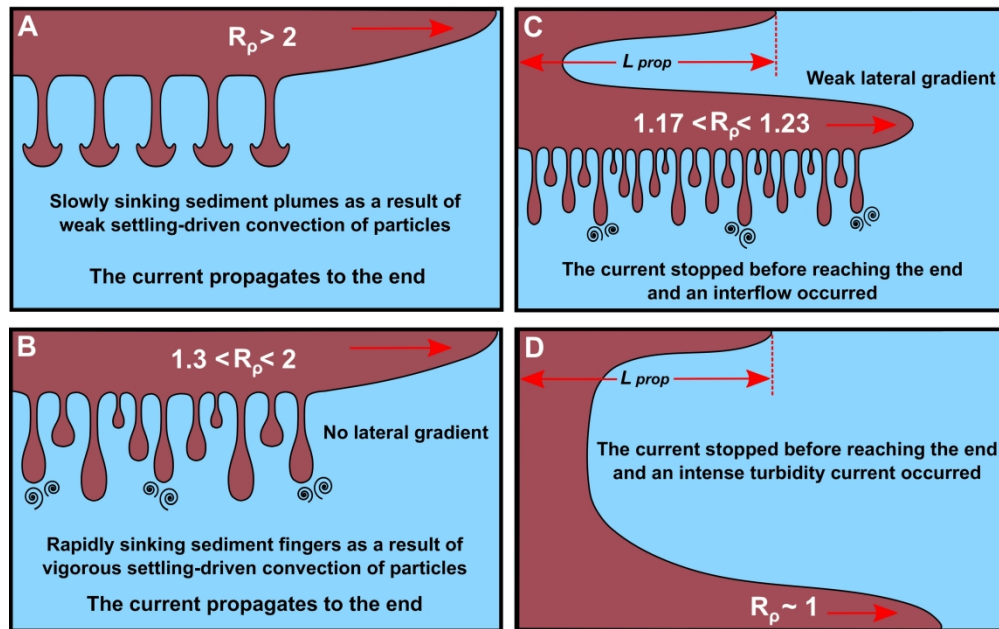
507x242mm (300 x 300 DPI)

Fig. 9: Schematic figure summarizing the four main modes of convection that arose in the current experiments. (A) Slowly sinking sediment plumes for $R_\rho > 2$, where weak settling-driven convection occurred and the current propagated to the end of the tank, (B) rapidly sinking sediment fingers for $1.3 < R_\rho < 2$, where vigorous settling-driven convection occurred and the current propagated to the end of the tank, (C) occurrence of an interflow for $1.17 < R_\rho < 1.23$, where the surface plume stopped before reaching the end of the tank and (D) occurrence of an intense turbidity current for $R_\rho \sim 1$, where the surface plume did not reach the end of the tank.
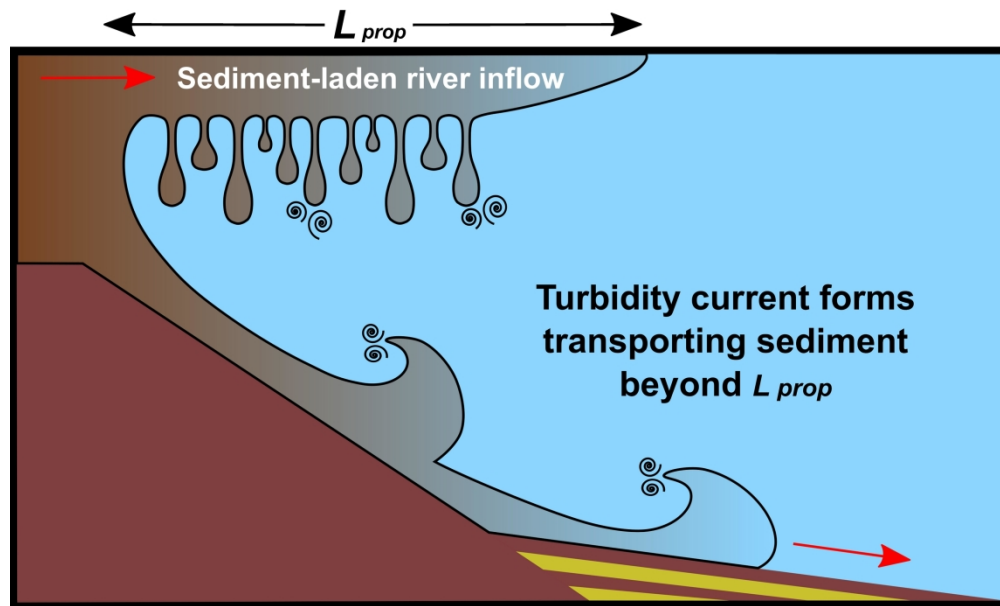
319x202mm (300 x 300 DPI)

Fig. 10: The rapid loss of sediment from the surface gravity current can potentially form a turbidity current that can transport sediment particles and propagate distances much greater than L_{prop}. This is the more likely behavior when R_ρ is close to 1. The new experiments in this paper now suggest that Figure 1 is more relevant only for very large density ratios.
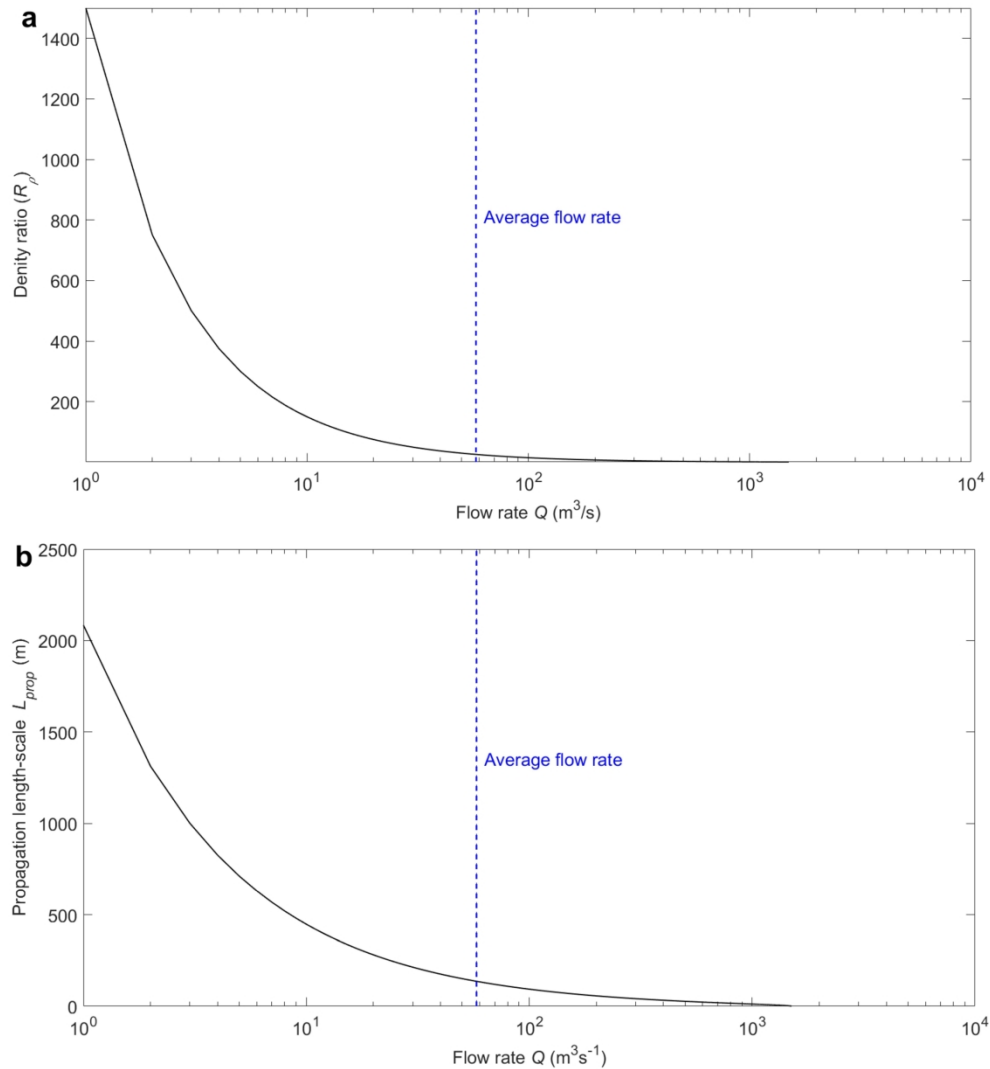
285x170mm (300 x 300 DPI)

Fig. 11: The scaling for the propagation distance can be applied to sediment-laden rivers, if the sediment load is known. (A) The predicted density ratio (R_ρ) as a function of the flow rate (Q) for the Squamish River, using Equation (15) and data from Mulder & Syvitski (1995). For high values of flow rate, the density ratio is less than one, implying the river can form a plunging flow. For lower flow rates, the density ratio can be much greater than one, as the density difference due to the added sediment is now less than the density difference between fresh and salty water. (B) The predicted propagation length-scale (L_{prop}) is plotted as a function of flow rate values (Q) using Equation (11). For values of flow rate greater than 1500 m^3 s^{-1}, L_{prop} = 0 as a plunging flow would form. For lower flow rate values the concentration of suspended sediment decreases, so that L_{prop} increases with decreasing Q.

201x216mm (300 x 300 DPI)